ACTIVE FLOW CONTROL IN AN ADVANCED SERPENTINE JET ENGINE INLET DUCT

A Thesis

by

AARON MICHAEL KIRK

Submitted to the Office of Graduate Studies of
Texas A&M University
in partial fulfillment of the requirements for the degree of

MASTER OF SCIENCE

December 2006

Major Subject: Aerospace Engineering

ACTIVE FLOW CONTROL IN AN ADVANCED SERPENTINE JET ENGINE INLET DUCT

A Thesis

by

AARON MICHAEL KIRK

Submitted to the Office of Graduate Studies of
Texas A&M University
in partial fulfillment of the requirements for the degree of

MASTER OF SCIENCE

Approved by:

Chair of Committee,	Othon K. Rediniotis
Committee Members,	Rodney D.W. Bowersox
	Luis San Andres
Head of Department,	Helen L. Reed

December 2006

Major Subject: Aerospace Engineering

ABSTRACT

Active Flow Control in an Advanced Serpentine Jet Engine

Inlet Duct. (December 2006)

Aaron Michael Kirk, B.S., Texas A&M University

Chair of Advisory Committee: Dr. Othon K. Rediniotis

An experimental investigation was performed to understand the development and suppression of the secondary flow structures within a compact, serpentine jet engine inlet duct. By employing a variety of flow diagnostic techniques, the formation of a pair of counter-rotating vortices was revealed. A modular fluidic actuator system that would apply several different methods of flow control was then designed and manufactured to improve duct performance. At the two bends of the inlet, conformal flow control devices were installed to deliver varying degrees of boundary layer suction, suction and steady fluid injection, and suction and oscillatory injection. Testing showed that suction alone could delay flow separation and improve the pressure recovery of the duct by as much as 70%. However, this technique was not able to rid the duct completely of the nonuniformities that exist at the engine face plane. Suction with steady blowing, however, increased pressure recovery by 37% and reduced distortion by 41% at the engine face. Suction with pulsed injection had the least degree of success in suppressing the secondary flow structures, with improvements in pressure recovery of only 16.5% and a detrimental impact on distortion. The potential for gains in the aerodynamic efficiency of serpentine inlets by active flow control was demonstrated in this study.

DEDICATION

I dedicate this thesis to my wife, Alison, and my parents, Gary and Sharon Kirk. Their constant love and support over the years has allowed me to reach this level in my career.

ACKNOWLEDGMENTS

I would like to thank Dr. Othon Rediniotis for allowing me to contribute to this project and for his continual guidance in my education and research. I also thank my committee members, Dr. Rodney Bowersox and Dr. Luis San Andres, for their support and advice.

I extend thanks to my fellow graduate students involved in this project, Nathan Tichenor and Abhinav Kumar. Their assistance in nearly every phase of this research endeavor has contributed to its success. Additionally, I would like to thank Dr. Lance Traub, whose expert knowledge and advice on experimental aerodynamics has been invaluable.

I thank the technical staff of the Texas A&M University Aerospace Engineering Department, Josh Wiemar and Rick Allen, for their help in the fabrication of the many complex parts that this project required.

Finally, I would like to thank Dr. Rhett Jeffries from the Air Force Office of Scientific Research for the generous grant that allowed this research to be possible.

TABLE OF CONTENTS

Page

ABSTRACT iii

DEDICATION iv

ACKNOWLEDGMENTS v

TABLE OF CONTENTS vi

LIST OF FIGURES vii

LIST OF TABLES ix

INTRODUCTION 1

General 1
Previous Work 3

EXPERIMENTAL SETUP AND PROCEDURES 11

Compact, Serpentine Jet Engine Inlet Duct 11
Wind Tunnel Facilities 16
Data Acquisition 17
Fluidic Actuator 27

RESULTS AND DISCUSSION 38

Bench Top Fluidic Actuator Performance 38
Baseline Duct Model 43
Flow Control – Suction 50
Flow Control – Suction and Steady Blowing 54
Flow Control – Suction and Pulsed Blowing 59

CONCLUSIONS AND RECOMMENDATIONS 64

Conclusions 64
Recommendations 66

REFERENCES 67

VITA 70

LIST OF FIGURES

Page

Figure 1: Secondary Flow Development at the Bends of a Serpentine Duct 4

Figure 2: Illustration of the Vortex Production by Straight and Angled Slots 9

Figure 3: Geometry of the Compact, Serpentine Inlet Model Used in this Study 12

Figure 4: Baseline Duct Model 13

Figure 5: Molds Employed to Create Fiberglass Reproductions of the Inlet Duct 14

Figure 6: A Set of Fiberglass Duct Sections for the Integration of Flow Control 15

Figure 7: Experimental Setup for Duct Testing 17

Figure 8: ESP Pressure Scanner for the Rapid Acquisition of Multiple Pressures 18

Figure 9: 32-Port Probe Rake for Engine Face Pressure Surveys 21

Figure 10: Data Points Conforming to the ARP1420 Guidlines 23

Figure 11: Seven-Hole Probe Mounted in the Sting 24

Figure 12: Probe Data Acquisition Grid 25

Figure 13: Schematic of the Fluidic Actuators 30

Figure 14: Centrifugal Fan and Fan Housing 31

Figure 15: First and Second Bend Suction Plenum Chambers and Fan Compartments 31

Figure 16: Slotted Shaft Valves Linked with Universal Joints 32

Figure 17: Slotted Shaft Valve Installed in a Blowing Plenum Chamber 33

Figure 18: Assembled First and Second Bend Blowing Plenum Components 34

Figure 19: Entire First Bend Flow Control Actuators 34

Figure 20: Electric Motors Used to Drive the Fans (Left) and Slotted Shaft Valves (Right) 36

Page

Figure 21: Schematic of the Control and Acquisition Setup....37

Figure 22: Steady Blowing Jet Velocity Calibration 39

Figure 23: Unsteady Fluidic Actuator Performance 41

Figure 24: FFT of the Jet Velocity at a Fan Speed of 15,000 RPM and a Pulsing Frequency of 100 Hz 41

Figure 25: Average Jet Velocity of the Oscillating Actuator at Various Fan Speeds....42

Figure 26: Pressure Contours within the Duct Resulting from CFD Analysis 44

Figure 27: CFD Streamline Trace 45

Figure 28: First Bend Surface Flow Visualization....47

Figure 29: Second Bend Surface Flow Visualization 47

Figure 30: Wall Static Pressure Distribution of the Baseline Duct Model 48

Figure 31: Engine Face Total Pressure Loss Coefficient Contour Plot with Velocity Vectors 49

Figure 32: Comparison of Baseline and Suction Flow Control Wall Static Pressures 52

Figure 33: Pressure Loss Coefficient Contour Plots Comparing Various Amounts of Suction Flow Control (Right Half) to the No Control Case (Left Half) 53

Figure 34: Pressure Loss Coefficient Contour Plots Comparing Various Amounts of Steady Injection (Right Half) to the No Control Case (Left Half)....56

Figure 35: A Plot of the Duct Performance Parameters for Different Methods and Levels of Control....57

Figure 36: C_{Ploss} and Velocity Vectors of the Duct with No Control (Left Half) and with Steady Suction and Injection (Right Half) 59

Figure 37: FFT of the Pressure at the Engine Face Plane 61

Figure 38: Pressure Loss Coefficient Plots Comparing Various Frequencies of Pulsed Injection (Right Half) to the No Control Case (Left Half) 63

LIST OF TABLES

Page

Table 1: Average Coefficient of Pressure Loss and Distortion Descriptor Values Obtained with Suction Flow Control 53

Table 2: Effects of Steady Blowing Flow Control on the Duct Performance Descriptors 55

INTRODUCTION

General

Current trends in the advancement of U.S. military air superiority require aircraft that emit low radar and infrared signatures. With regards to propulsion, this need for stealth capabilities has led to the development of serpentine inlet ducts. These S-shaped ducts do not provide a direct line of sight to the compressor blades, thus hiding the engine from incoming radar waves. Also, serpentine inlets allow for buried engines, which can help shield the infrared signature of high-temperature exhaust gases.

In addition to the benefits of low observability provided by serpentine ducts, these jet engine inlets also allow for reductions in vehicle size due to their axially compact geometries. This advantage is particularly important in unmanned aerial vehicles (UAV's). A scaling analysis performed by engineers at Lockheed Martin showed that reducing duct length by one duct diameter can decrease the empty weight of UAV's by 15%[1]. In typical aircraft, the cockpit and associated life support and pilot interface systems make up a significant portion of the fuselage, thus reducing the importance of the jet engine inlet length in the overall design of the vehicle. However, for unmanned aircraft, where these components are not present, the length of the engine inlet can drive the fuselage size. Therefore, for such airplanes, the utilization of compact jet engine inlet ducts can lead to smaller aircraft with decreased vehicle and operating costs.

This thesis follows the format of the *AIAA Journal.*

Unfortunately, these duct geometries are conducive to the emergence of significant secondary flow structures, leading to large amounts of pressure loss and flow distortion. Poor pressure recovery results in reduced overall engine performance and decreased fuel efficiency, while distortion at the engine face plane causes instabilities in the compressor dynamics that lower engine surge and stall limits[1,2,3]. Additionally, the circumferential distortion pattern acts as an unsteady forcing function, inducing blade vibration that can result in structural fatigue and failure[3]. This shortcoming occurs when the rotor blades pass through regions of reduced axial velocity (i.e., where the total pressure is low). In these areas, since the flow velocity component due to rotation becomes greater with respect to the axial component, the blade incidence angle is increased. Much like the stalling of an airfoil at high angles of attack, the flow over the blade separates at these large incidence angles. This action changes the loading on the blade and creates flow instabilities that convect through the later compressor stages.

This thesis presents a study performed to gain an understanding of the development and control of secondary flows that hinder the performance of compact, serpentine jet engine inlet ducts. Using a variety of methods, such as a survey of previous literature on the subject, computational fluid dynamics (CFD) analysis, flow visualization tests, and pressure probe and wall static tap experiments at various locations, the development and evolution of the secondary flow structures were observed. With this information, flow control devices were designed and constructed to control and suppress secondary flows and eliminate the associated pressure loss and flow nonuniformities that are detrimental to engine performance. The results of this effort

will be presented using a variety of industry standard performance descriptors that allow quantification of the gains achieved by flow control.

Previous Work

Many investigations have explained the development of the secondary flow in serpentine ducts, which is characterized by a pair of large, counter-rotating vortices[4,5,6]. When negotiating a bend, a centrifugal force is generated on the core flow, causing it to accelerate. This action, in conjunction with flow separation towards the inner region of the bend, produces a pressure differential, by which the pressure at the inside of the bend is lower than that at the outside of the bend. The consequence of this cross-stream pressure inconsistency is migration of the boundary layer flow towards the center of the duct, where the merging flow is pushed away from the wall and back towards the outside of the bend. From this motion, the lift-off of two counter-rotating vortices is produced. An illustration of this process is shown in Figure 1. To supplement this description, another study added that the low momentum fluid that converges at the duct centerline thickens the local boundary layer[7]. Therefore, its ability to endure adverse pressure gradients is reduced and flow separation is further encouraged. In the Results and Discussion section of this thesis, photographs and plots provide a visual and quantitative view of the above discussion regarding secondary flow development.

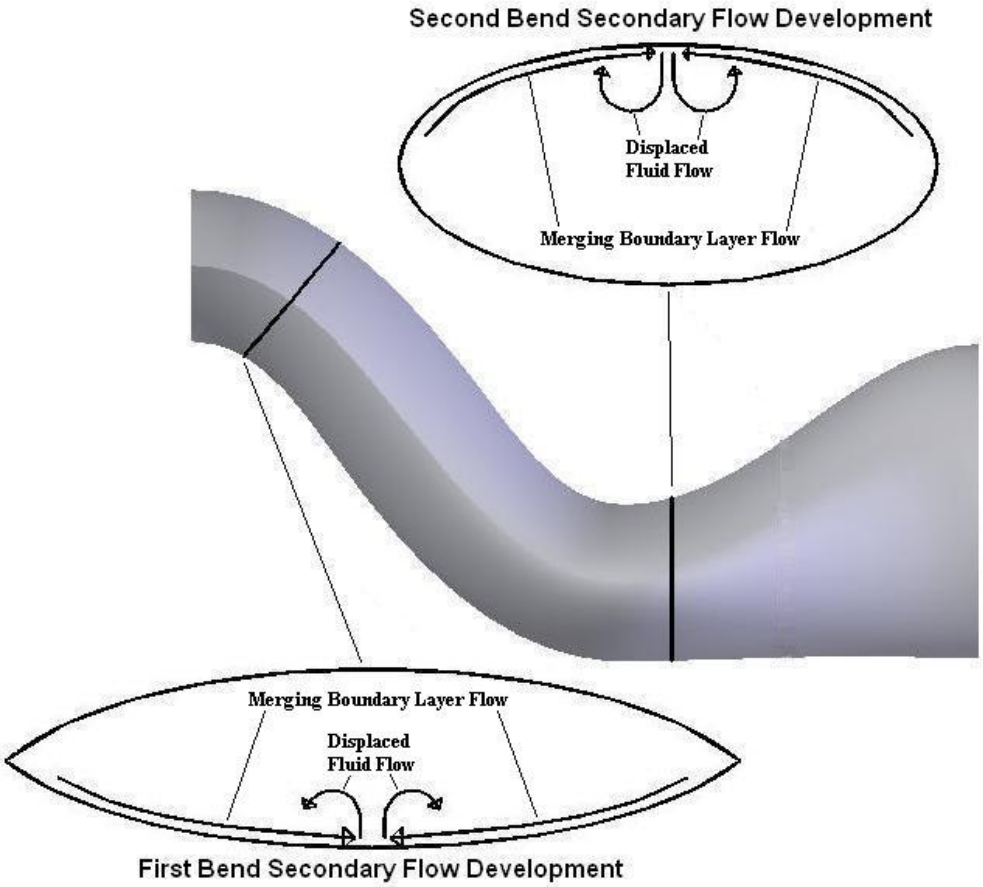

Figure 1: Secondary Flow Development at the Bends of a Serpentine Duct

In general, there are two techniques that govern the flow control methods used to combat the nonuniform flows and decreased pressure recovery associated with serpentine ducts. One aims to use vane or jet vortex generators to mix the high energy core flow with the low momentum boundary layer flow, thus suppressing flow separation. This approach, as showcased in studies by Reichert and Wendt[8], Tindell[9], and Kumar and Alvi[10,11], may be successful in eliminating the pressure loss associated with flow separation, however, it is not ideal for reducing distortion at the engine face. Instead, the goal of the second technique is to globally restructure the secondary flows

by using vortex generators to counter the merging boundary layer fluid and spread it evenly around the duct periphery[1,2,5]. This method increases pressure recovery and lessens the nonuniformities in the flow. The research presented in this thesis will concentrate on the latter approach.

To date, many related studies have been performed on the topic of flow control in diffusing S-ducts. The majority of the past research has utilized passive flow control methods, such as vortex generators. Passive control devices are a popular choice for many researchers because they are simple, inexpensive, achieve reasonable results, and do not require the introduction of energy. Studies by Reichart and Wendt[5,8] explored the use of traditional vane vortex generators on a moderately curved duct with a diffusing, circular cross-section. The researchers investigated the effects of vane height, spacing, and axial location, and showed improvements in pressure recovery and distortion reduction in almost all cases. However, this duct, the M2129, had a far simpler flowpath than the one to be discussed in this thesis. In another set of experiments, Anabtawi et al.[2,4] showed that vane-type vortex generators were also successful in mitigating the pressure loss and nonuniformity in a boundary layer ingesting duct. Again, this inlet, which was designed for a blended-wing-body transport jet, had a much less aggressive geometry than that employed for this thesis.

Vortex generation via aerodynamic vanes in simple serpentine ducts has even transitioned to numerical research. Anderson and Gibb developed a mathematical model of the vortices shed from vanes and used CFD to explore several vane configurations at

different flight conditions in the M2129 duct[12]. They later compared their numerical results to experimental data and concluded that good agreement was achieved[13].

Although it has been proven reliable in the aforementioned studies, passive control by vortex generating vanes is not ideal because it can only be optimized to a certain flow condition, usually cruise. During other phases of flight, such as landing or takeoff where airspeeds are lower, or during maneuvers in which nonuniform flow can enter the duct, vortex generators may not be effective. An additional shortcoming of vane-type vortex generators is the risk of foreign object damage they pose[14]. Not only could external objects damage the vanes and render them aerodynamically useless or even detrimental, but the vanes themselves could become the foreign object if they were to break and be ingested by the engine. Also, vane vortex generators are not ideal because they have parasitic drag[10], which contributes to pressure loss, particularly at off-design conditions.

To avoid the problems associated with passive flow control devices, some studies have explored the use of active control technologies. Active flow control requires energy to be added to the system, which can increase complexity and cost. However, the advantage of having the ability to modify flow control parameters to yield desirable effects at all flight conditions without concern for foreign object damage or parasite drag outweighs this downside. An active flow control method investigated in many studies is steady blowing microjets. Kumar and Alvi[10,11] showed that supersonic jets of 400 μm diameter were successful in preventing flow separation. They explored the effects of different amounts of momentum injection, microjet array locations, and microjet angles

on flow separation. However, the geometry used in that study was a simple, two-dimensional ramp with gentle curvature called a Stratford ramp. During a research project at Virginia Polytechnic Institute and State University, separate tests were performed using suction, blowing, and suction and blowing together on a diffusing, S-duct with a rectangular cross-section[15]. Here, a zero net mass flux actuator was simulated and proved successful in enhancing the performance of the duct. As in the above study, though, the test article was not representative of a modern serpentine inlet. Additionally, only one type of orifice arrangement and control mass flow was investigated.

In these microjet studies, the focus of the flow control was to prevent separation. Therefore, based on the results obtained, it is difficult to determine whether microjets would have any significant authority in restructuring the secondary flows in a serpentine inlet. However, in the investigation performed by Hamstra et al.[1], countering the secondary flow structures was the primary motivation behind the use of microjets to improve pressure recovery and distortion in a highly serpentine and compact duct. Here, the researchers used the concept of vorticity signature in designing their vortex generating jets. Vorticity signature is a principle that states that the strength, distribution, and secondary flowfield interaction of the vortices generated by flow control devices are the primary means by which secondary flow control is achieved. This study was performed at realistic flight conditions and utilized a realistic flowpath, but never fully succeeded in preventing the large, counter-rotating vortices from developing. Additionally, only steady blowing jets were used. No investigation was

launched to determine the effect of pulsed blowing on the separation and secondary flow development.

In all of the microjet research discussed above, the jets were formed through tiny holes only. No effort was made into exploring other orifice geometries or configurations, such as slots angled laterally to the freestream. This fact could explain the ineffectiveness of such microjets in restructuring the secondary flow. Figure 2 illustrates the dynamics of the flow when a perpendicular jet interacts with the duct core flow. A pair of streamwise, counter-rotating vortices develops directly above the jet that enhances mixing of the high-energy freestream flow and the low-energy boundary layer fluid. This mixing delays or prevents flow separation, but the counter-rotating vortices are usually equal in strength. Therefore, no net vorticity is created that could redirect the merging near-wall flow. This is not the case with traditional vane-type vortex generators, which only create a single vortex.

Thus, to achieve the objective of reducing pressure loss and flow distortion, it may be necessary to orient the jet slots in such a way as to create a single vortex. Bridges and Smith showed that a lone vortex could be achieved by orienting the jet slot at an angle to the streamwise direction[16]. In this situation, the jet fluid emerges from the slot perpendicular to the freestream in similar fashion to the jet described previously. However, since the broad side of the jet is exposed to the oncoming core flow, the upstream side vortex formation is impeded while the downstream side vortex is exacerbated. As the orientation angle of the slot is increased, so too is this effect. Also, the penetration depth of the jet into the freestream flow decreases with larger slot angles.

The consequence of this effect is a more oblong vortex located closer to the wall, as shown in Figure 2.

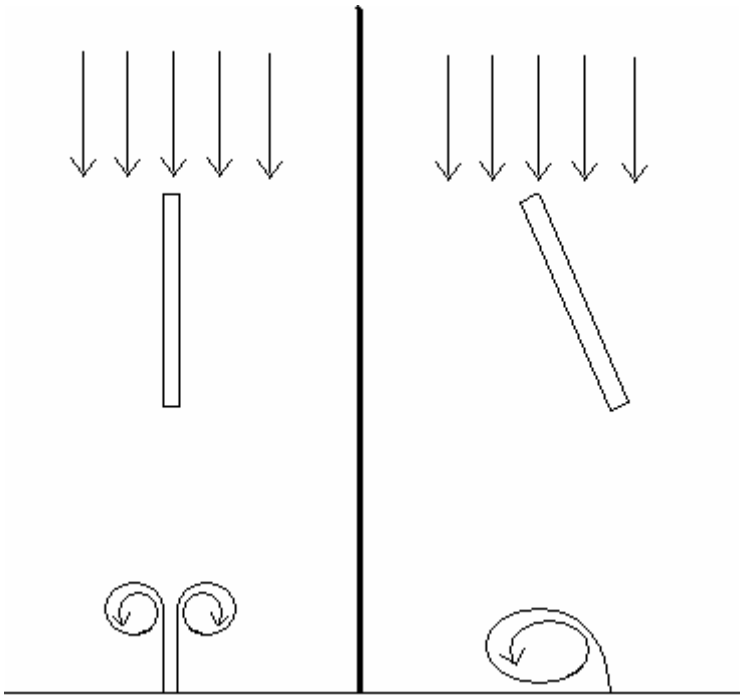

Figure 2: Illustration of the Vortex Production by Straight and Angled Slots

Although microjets may prove useful in improving serpentine duct performance, there are aspects that make them less advantageous when compared to zero mass flux devices, such as synthetic jet actuators (SJA). For one, microjets require an external flow source, such as bleed air from the engine compressor. Not only does this take away from the efficiency of the engine, but the addition of a complicated plumbing system to deliver compressed air to the appropriate location would add weight, size, and cost to the aircraft. Also, maintenance on this plumbing could be very difficult. A team of researchers at North Carolina State University designed a bleed air system that added approximately 3% to the empty weight of a scaled UAV designed by NASA and

Lockheed Martin[17]. To cool the bleed air for injection into the inlet duct, the piping had to be coiled and placed in the fuel tank, which would contribute greatly to maintenance complexity.

Synthetic jet actuators have the potential to reduce pressure loss and flow distortion in S-shaped inlet ducts without the negative aspects of the flow control technologies described above. These systems are usually compact and require little, if any, communication or connection to remote hardware[18]. Much of the research has applied SJA's to the suppression of separation and improvement of stall characteristics for airfoils and bluff bodies, as described in publications by Gilarranz and Rediniotis[18], Gilarranz et al.[19], Seifert and Pack[20], and Glezer[21]. In these studies, actuators with spanwise slots utilizing tangential blowing with respect to the wing surface were able to prevent separation over the upper surface for very large angles of attack, thus improving the stall threshold of the airfoils. Amitay et al.[22] shifted this thinking to internal flows, using an SJA array to delay separation in a rectangular, diffusing duct. This study was successful in achieving its goal, but had no correlation to secondary flow suppression in highly three-dimensional inlets.

EXPERIMENTAL SETUP AND PROCEDURES

In this section, the experimental equipment utilized for this research endeavor will be described. The features of a serpentine jet engine inlet will be discussed, followed by an explanation of the methods used to obtain and manufacture the duct. Also, the wind tunnel test facilities will be presented with a look at the data acquisition hardware and software. Lastly, a new flow control actuator, designed specifically for this project, will be characterized.

Compact, Serpentine Jet Engine Inlet Duct

Duct Geometry

To investigate the development and evolution of secondary flows and how to suppress them, an axially compact, three-dimensional S-duct was employed. The duct was designed at Lockheed Martin for use in next-generation UAV applications, and was the test article of the study reported by Hamstra et al[1]. The inlet model, which can be viewed in Figure 3, features two, approximately 45 degree bends, and an elliptical-to-circular, diffusing exit section. The exit diameter is 25.4 cm and the overall duct length is 63.5 cm, yielding a length-to-diameter ratio (L/D) of 2.5. At this size, the inlet duct is approximately 40-50% scale for a typical UAV. A biconvex entrance section measuring 25.4 cm in length with an aspect ratio of 4 was added upstream of the first bend to simulate the boundary layer development over a fuselage forebody. Also, for smooth ingestion of the ambient air, a bellmouth contraction with an area ratio of 7.4 was

utilized. This addition prevents the flow from separating over the inlet lip as it enters the duct and helps produce a uniform flowfield.

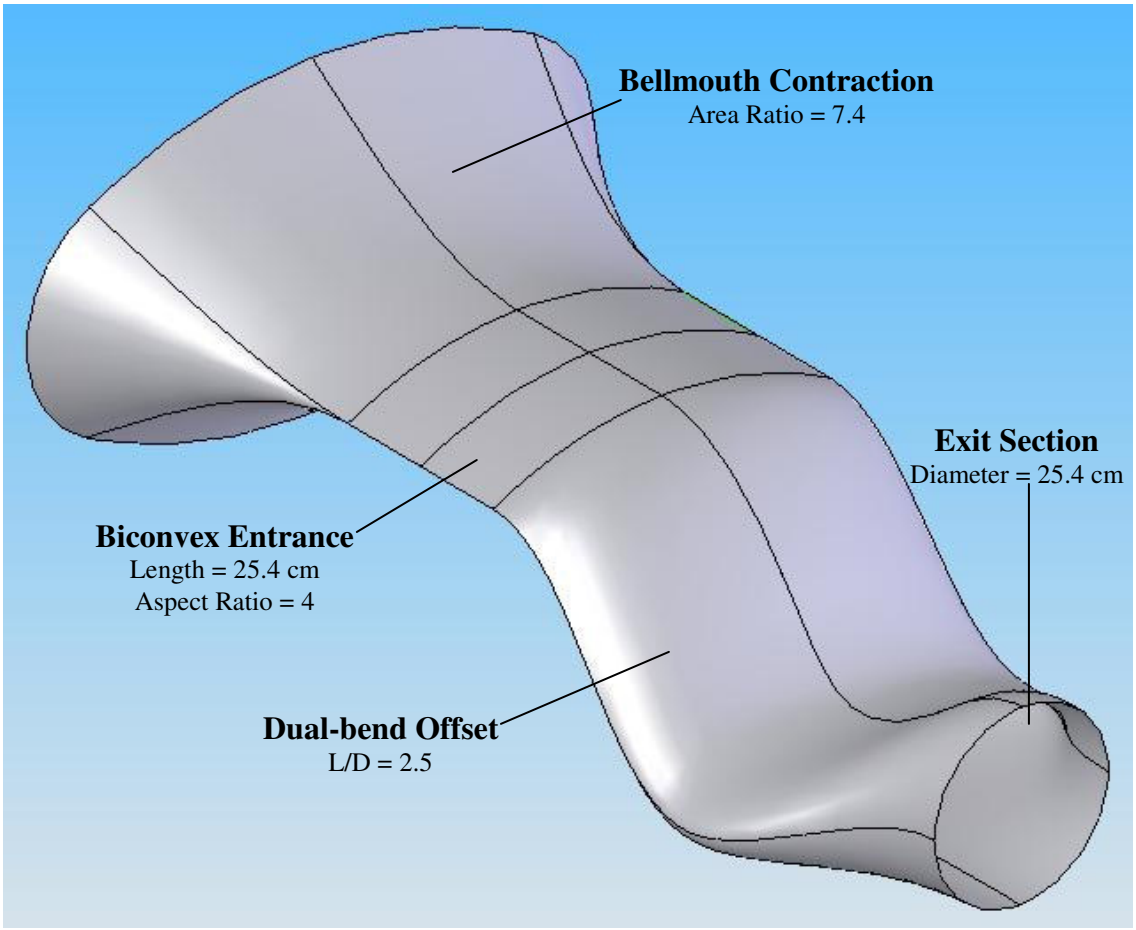

Figure 3: Geometry of the Compact, Serpentine Inlet Model Used in this Study

Baseline Duct Model

Initial testing was performed on a baseline duct model donated to the Texas A&M University Aerospace Engineering Department by Lockheed Martin Aeronautics Company in Ft. Worth, Texas. The duct was fabricated through a laser stereo-lithography (SLA) process and consists completely of hardened resin[1]. The model is split into seven modules to accommodate interchangeable flow control blocks. Flanges

house grooves for o-ring placement and allow the modules to be bolted together to quickly assemble and disassemble the duct. Pressure taps incorporated along the centerline of both the top and bottom walls allow surface static pressures to be obtained. A photograph of this SLA constructed, resin inlet model is presented in Figure 4.

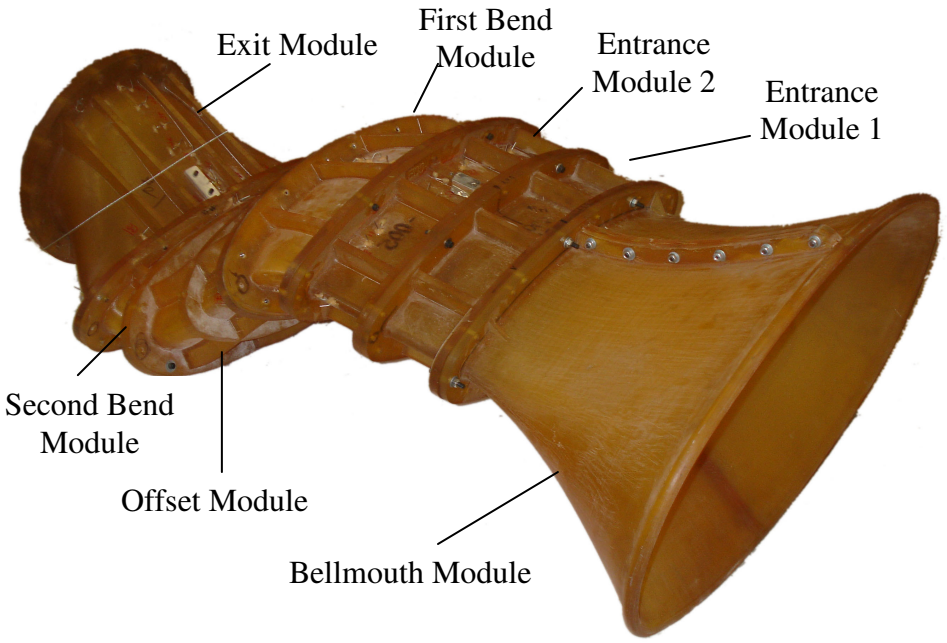

Figure 4: Baseline Duct Model

Flow Control Duct Model

After the locations of flow separation and vortex lift-off were determined, several of the duct modules were reconstructed to allow the integration of newly designed fluidic actuators for flow control. Rebuilding the inlet was chosen over modifying the existing sections due to the difficulty of machining the brittle resin. Several technologies were considered for the fabrication of the replica, including rapid prototyping by stereo-lithography or fused deposition modeling, computer numerical control (CNC) machining, injection molding, and sheet metal forming. However,

because of budget concerns, a more economical method involving fiberglass with wood reinforcement was elected.

This manufacturing technique began with the creation of reusable, fiberglass molds. The resin duct model from Lockheed Martin was used as a basis for these molds. Clear packaging tape was applied to the inside surface of each module to create a layer of separation and prevent the fiberglass epoxy from adhering to the walls. Then, a layer of woven fiberglass cloth was spread over the taped surface and a two-part epoxy compound was brushed into the cloth. To ensure that the shape of the cured fiberglass would hold after being removed from the duct walls, three layers of fiberglass cloth were used. After hardening, imperfections in the fiberglass pieces were repaired with body filler and sanded until smooth. As a finishing step in preparing the molds, about three coats of primer were sprayed on the surfaces. This process was performed separately for the top and bottom surfaces of each module. Then, the halves of the molds were joined, and plastic extensions for the fabrication of flanges were added. Figure 5 shows the completed molds.

Figure 5: Molds Employed to Create Fiberglass Reproductions of the Inlet Duct

The next phase in the construction of the duct model with flow control capabilities started with the application of wax and a polyvinyl alcohol (PVA) release film. This step was necessary to ensure easy release of parts from the molds. Approximately four layers of the fiberglass cloth were then applied to the molds, followed by two layers of unstructured, fiberglass matting. The thin, woven cloth was much easier to shape than the matting, but was far weaker. Therefore, the combination of the two fiberglass raw forms provided accurate and smooth, yet stiff replicas of the duct modules. For further strengthening, wooden ribs were integrated in the layers of fiberglass matting, as were wooden flanges for connecting adjacent sections. Rubber gasket material was compressed between the flanges during assembly to prevent leakage. In similar fashion to the original resin duct from Lockheed Martin, static pressure taps were added along the centerline of the top and bottom walls. The completed fiberglass modules can be seen in Figure 6.

Figure 6: A Set of Fiberglass Duct Sections for the Integration of Flow Control

Wind Tunnel Facilities

For testing, the inlet models were integrated into an open-circuit, suck-down wind tunnel with a 0.4572 m x 0.4572 m, square cross-section. To connect the circular exit of the inlet duct to the square wind tunnel, a fiberglass diffuser was built. Upstream of the diffuser, a rubber pipe coupler was utilized to isolate the duct from vibrations produced by the wind tunnel fan. The coupler was clamped to a steel pipe to which the exit section of the duct was mounted. A slot with a width of 25 cm that spanned half the circumference was cut from the pipe to allow probe access. The pipe rested upon an adjustable stand, thus providing vertical support for the downstream portion of the inlet model. To add a rigid brace to the opposite end of the duct, a steel frame was bolted between the flanges of the bellmouth and first entrance modules. The frame legs consisted of square pipe, and were welded to a quarter-inch sheet machined by CNC to conform to the inner surface of the duct and the hole locations of the flanges. In Figure 7, the serpentine inlet experimental setup is pictured.

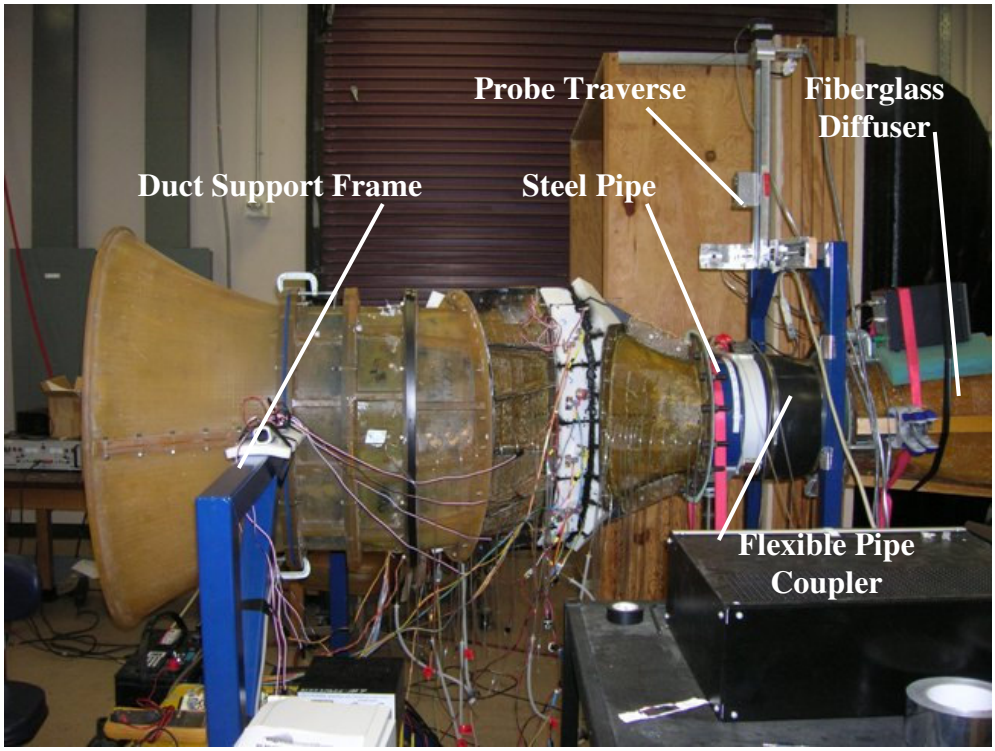

Figure 7: Experimental Setup for Duct Testing

Flow through the tunnel was driven by a large, centrifugal blower measuring 0.6096 m in diameter. Maximum velocity through the duct, measured with a Pitot tube in the second entrance module, was approximately 65 m/s. This value corresponds to a Mach number of 0.19, a Reynolds number based on exit diameter of 1.1×10^6, and a mass flow rate of 3.3 kg/s.

Data Acquisition

Electronic Pressure Scanner

The majority of the data obtained for this document was collected through the use of a miniature, 32-port, electrically scanned pressure (ESP) device from Pressure Systems, Inc. The ESP scanner, shown in Figure 8, was employed for gathering

pressures from the wall static taps, a seven-hole probe, and a 32-point probe rake. The advantage of this sensor array is the rapid acquisition of all 32 ports. The sensors of the pressure scanner are digitally multiplexed at rates up to 20,000 Hz. Therefore, over 600 samples of the entire array can be obtained every second. Additionally, another benefit is the pneumatically actuated manifold inside the device that connects all 32 sensors to a single port to allow quick and easy calibration. The accuracy of the sensors in the pressure scanner is 0.05% of full scale, or 0.019 torr. The measurement uncertainty using the ESP scanner with the various flow diagnostic devices will be discussed later.

Figure 8: ESP Pressure Scanner for the Rapid Acquisition of Multiple Pressures

To interface with the ESP scanner, special hardware is required to supply power and perform the digital addressing. For the project presented in this thesis, the hardware was provided by the Aeroprobe Corporation. Controlled by a PC using special software, the mechanism provided pressure for pneumatic actuation of the ESP manifold and for sensor calibration. The device also converted the digital output of the PC to CMOS logic for port addressing.

Acquisition Software

Aeroprobe also supplied software for use with the pressure scanner and associated hardware. This powerful program, called AeroAcquire, allows the user to control the acquisition of pressures from the ESP system or from individual sensors. It also performs automated calibration and, periodically, zero-offset adjustments for the sensors. Within the program, sampling rate and the number of samples can be adjusted, as can the number of ports to address. Unless otherwise stated, all pressure data gathered for this study was done so for 10 seconds at a 256 Hz sampling rate. The software can accommodate multiple ESP scanners as well as multiple pressure and fast response probes. Probe calibration files can even be loaded into the program for real-time data reduction, which involves the calculation of total pressure, static pressure, and the three velocity components from the individual port pressures. With AeroAcquire, the user also has the ability to load or generate a data acquisition grid and autonomously traverse a probe through the grid by utilizing the stepper motor control aspect of the software. The program can then output files containing time-series and averaged values of the raw pressures and reduced velocities at each point.

Static Pressure Taps

Surface static pressure can provide a great deal of insight into determining the regions of separated and attached flow. Therefore, the aforementioned pressure taps integrated into both duct models were utilized in determining the nature of the near-wall flow along the center of the duct for controlled and uncontrolled flow. Tygon tubing

connected the taps to the ESP pressure scanner, allowing the simultaneous collection of static pressures from the entire top or bottom surface.

Probe Rake

Data collected at the engine face plane is traditionally the primary means of analyzing the performance of a jet engine inlet. Most importantly, the total pressure variation at this location determines if the flow structures created within the inlet duct will have an adverse effect on engine performance. To acquire total pressure values in a quick and efficient manner, a rake consisting of 32 total pressure probes was designed and constructed. The apparatus was comprised of two perpendicular arms, each with 15 stainless steel tubes measuring 1.5875 mm in diameter. At a radial location of 69.85 mm, stand-alone pressure sensors with high frequency response capabilities were installed to obtain frequency content of the flow. The sensors were sampled at 1,024 Hz for 10 seconds. Their position was chosen from initial experiments, which showed that the vortex cores were in close proximity. Tygon tubing was attached to the probes and routed through the outer rim of the rake to the ESP pressure scanner located outside the tunnel. The rim, which was fit into a groove cut from the steel pipe, acted as a guide for manual rotation of the rake. A graduated scale was placed around the perimeter of the steel pipe to measure the angles of the rake arms. The uncertainty in the angular measurement was 0.5 degrees. The probe rake was only able to survey one half of the engine face plane. However, due to the symmetrical pattern of the flow, the pressures obtained were mirrored about the symmetry axis to provide a full set of engine face data. The probe rake is shown installed in Figure 9.

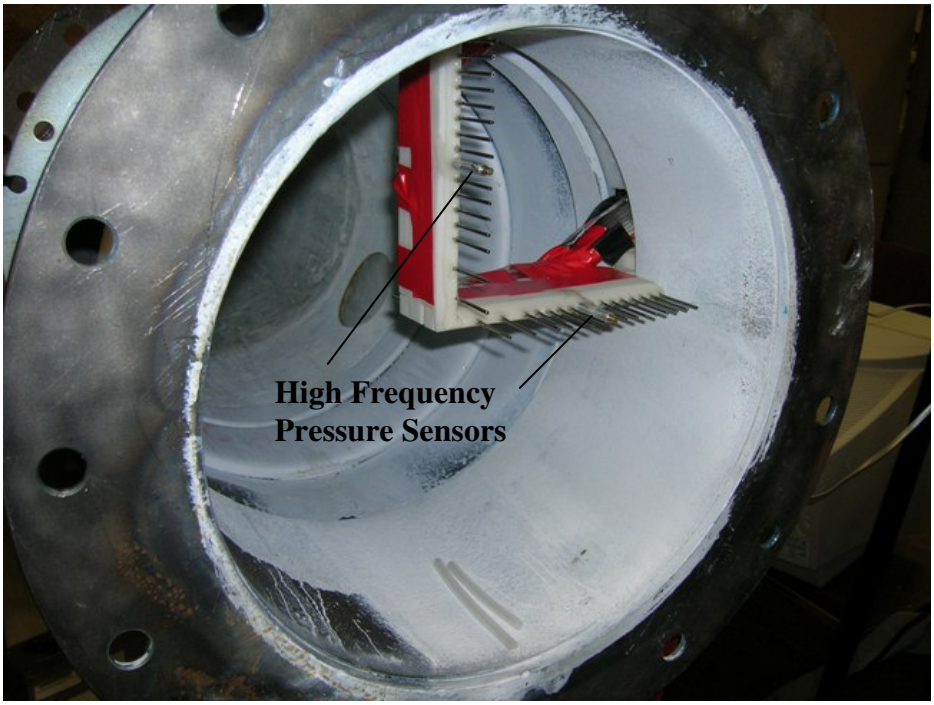

Figure 9: 32-Port Probe Rake for Engine Face Pressure Surveys

To evaluate the performance of the duct as well as the improvements achieved by the addition of flow control, some commonly used parameters must be introduced. First is the area-averaged coefficient of total pressure loss, denoted by $C_{Ploss,avg}$ and defined by Equation 1. This quantity provides a measure of the pressure recovery of the inlet.

$$C_{Ploss,avg} = \frac{P_{tot\infty} - P_{totef,avg}}{q_\infty} * 100 \qquad (1)$$

In the above equation, $P_{tot\infty}$ is the total pressure of the flow entering the duct, $P_{totef,avg}$ is the average of the total pressures acquired by the probe rake for the entire engine face, and q_∞ is the dynamic pressure of the flow entering the duct. Normalizing the coefficient by the dynamic pressure rather than the total pressure allows direct comparisons of the results at any freestream Mach number.

The distortion descriptor, DC_{60}, defined in Equation 2 is another parameter often used to analyze jet engine duct efficacy. This value quantifies the flow distortion at the engine face by comparing the minimum averaged total pressure over any 60 degree wedge, $P_{min60,avg}$, to the averaged total pressure over the entire engine face plane, $P_{totef,avg}$. For this thesis, the distortion descriptor is normalized by the area-averaged dynamic pressure at the engine face, $q_{ef,avg}$, and is expressed as a percentage. The report by Anabtawi et al. states that DC_{60} should be less than 20% to be considered acceptable[4].

$$DC_{60} = \frac{P_{totef,avg} - P_{\min 60,avg}}{q_{ef,avg}} * 100 \qquad (2)$$

In the calculation of DC_{60}, five of the probe rake's radial points were selected in accordance with the ARP1420[23]. This document of standards and practices from the SAE mandates that the probe locations lie at the centroids of rings equal in area. This concept is illustrated in Figure 10.

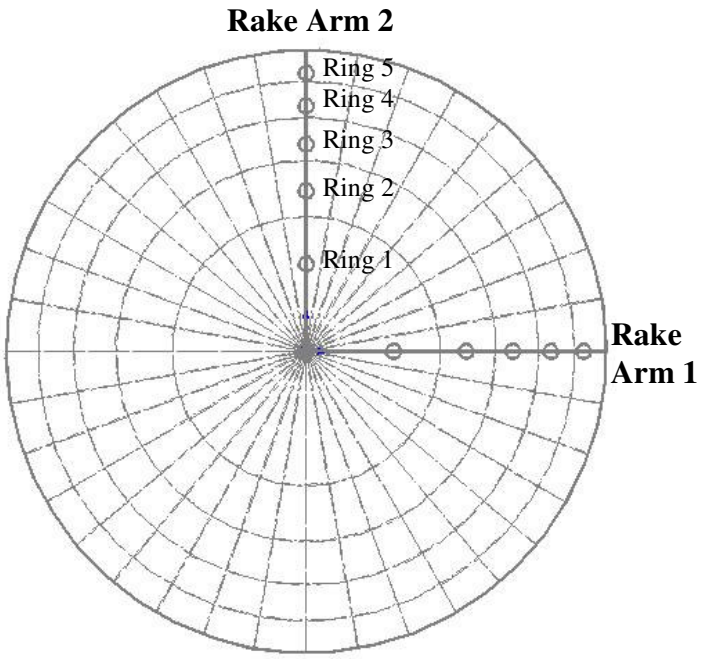

Figure 10: Data Points Conforming to the ARP1420 Guidlines

Seven-Hole Probe

To gather further information at the engine face, including static pressure and velocity magnitude and components, a miniature, seven-hole probe was utilized. The conical-tipped probe was manufactured at Texas A&M University and calibrated by the Aeroprobe Corporation. With seven pressure ports, the probe has the ability to accurately measure flow at angles up to 70 degrees. The tip diameter of the probe is a mere 1.5875 mm. This characteristic makes it ideal for the measurement of internal flows because flow blockage and disruption are negligible. Figure 11 presents a picture of the miniature probe.

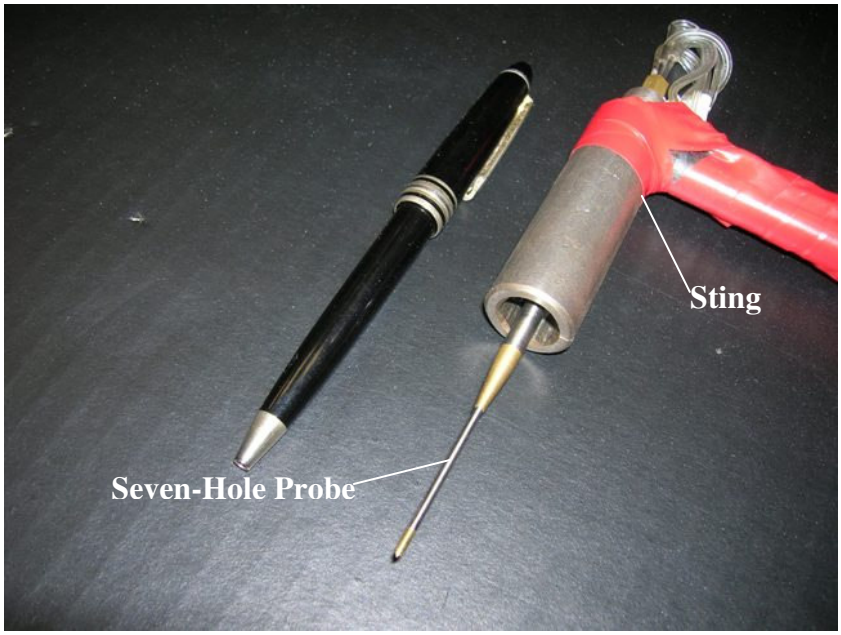

Figure 11: Seven-Hole Probe Mounted in the Sting

As discussed earlier, the AeroAcquire software can reduce the seven port pressures into static pressure, total pressure, velocity magnitude, and flow direction. The software utilizes a local least-squares reduction algorithm that compares parameters calculated from the seven pressures in the unknown flowfield to parameters calculated from a calibration file[24]. Given the density of the probe calibration file used for this project, Aeroprobe estimates that the uncertainty in the velocity magnitude and flow angles are 1.5% and 0.5 degrees, respectively.

To obtain a sufficiently dense survey of the flowfield at the engine face, the data acquisition grid illustrated in Figure 12 was employed. This grid puts the probe at 18 radial locations, spaced 6.35 mm apart, and 36 circumferential locations at 10 degree increments. In all, 648 points composed the data acquisition mesh.

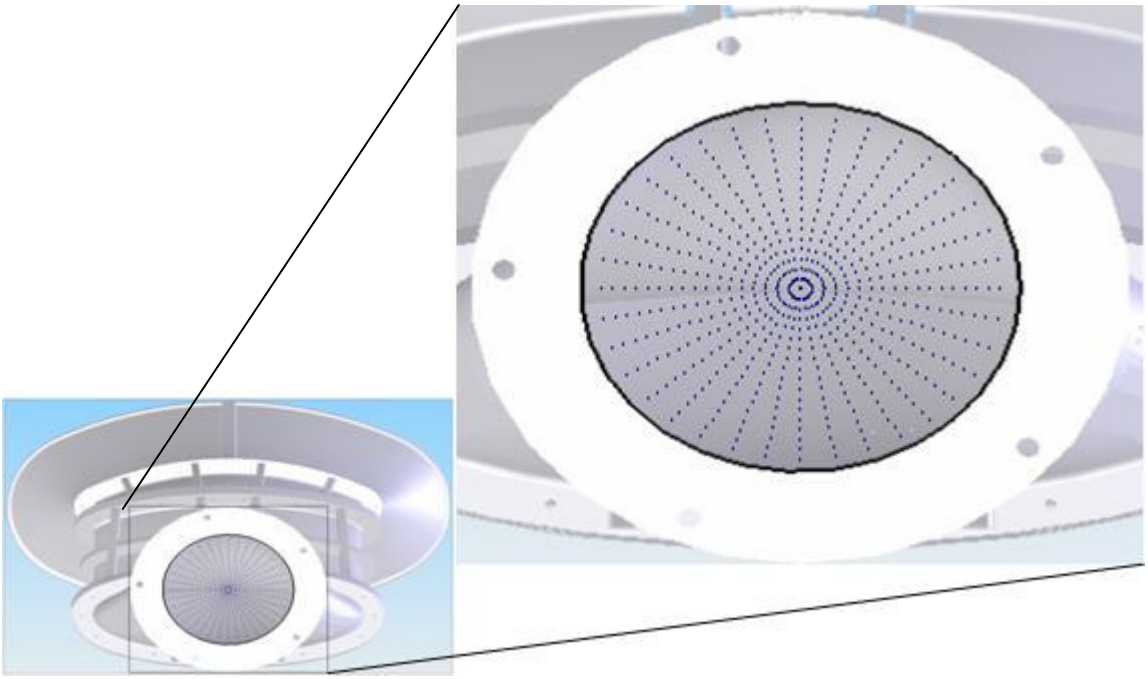

Figure 12: Probe Data Acquisition Grid

Probe Traverse System

The probe was positioned at the desired acquisition points using a two-axis, linear traverse. Lead screws with 20 threads per inch and Vexta stepping motors with a minimum step size of 1.8 degrees provided extremely accurate positioning down to 0.00635 mm. Stepper motor control hardware, which was furnished by the Aeroprobe Corporation, was interfaced with the grid acquisition feature of the AeroAcquire software for automated probe placement. Rotary encoders attached to the motors of each axis supplied feedback of the location. With this system, the uncertainty of the probe position was 0.009 mm.

The two-axis traverse apparatus was bolted to a steel frame that straddled the wind tunnel setup. A rigid, steel sting, to which the probe was mounted, extended downward from the traverse and through the slot in the steel pipe. A plastic ring with a

small hole to accommodate the sting was utilized to seal the large slot. The ring was guided by the aforementioned groove in the steel pipe and rotated in conjunction with probe movement to avoid contacting the sting. To view the probe traverse system, refer to Figure 7.

Uncertainty Analysis

Like all scientific measurements, the results in this thesis have some error that must be quantified to determine the confidence with which the measured values can be used to describe the true value of a quantity. Estimating this uncertainty is commonly done by combining the accuracy of the measuring system with the precision of the measurements. While the accuracy is often stated by the device manufacturer, precision error is associated with the random fluctuations and repeatability in the measurement and can be determined using the standard deviation of a set of data samples. Equation 3 shows how the uncertainty is calculated using this method.

$$u_i = \sqrt{a_i^2 + p_i^2} \tag{3}$$

In Equation 3, u_i is the total uncertainty in the measurement, a_i is the accuracy of the measurement device, and p_i is the precision of the measured value.

For this research endeavor, the standard deviation in the pressure measurements was determined through a repeatability study in which tests using the static pressure taps and engine face probe rake were repeated 10 times. Then, the precision was calculated by doubling the standard deviation, thus providing a 95% probability that the measurement was within the range of precision. Using this method, the average total

uncertainty in the static pressure tap measurements was 0.121 torr and the average uncertainty in the probe rake pressures was 0.161 torr.

When computing a quantity that is based on a measurement, the uncertainty in the measured value carries through the calculation process. To quantify this propagation, Kline and McClintock proposed the formulation for constant odds uncertainty predictions[25]. The constant odds approach states that if a parameter, R, is a function of the n number of measured, independent variables that have a Gaussian distribution, x_i, then the uncertainty of R can be calculated using Equation 4.

$$u_R = \sqrt{\sum_{i=1}^{n} \left(\frac{\partial R}{\partial x_i} u_{x_i} \right)^2} \tag{4}$$

In the above equation, u_R is the uncertainty of the calculated parameter and u_{xi} is the uncertainty in the measured value of x_i. In the Results and Discussion section of this thesis, the uncertainties calculated using the above techniques will be represented by error bars in the plots. Also, the errors of several calculated parameters will be displayed in the data tables.

Fluidic Actuator

Actuator Setup

A novel fluidic actuator system was designed and fabricated to apply flow control to the compact, serpentine inlet model. The flow control devices were based on the concept of the synthetic jet actuator in that they are closed systems that do not require external hardware such as plumbing for compressor bleed air. However, the

fluid actuators employed for this research are not true SJA's because they are modular. The term SJA refers to a zero net mass flux actuator in which the flow is alternately ingested and blown through a common orifice. These devices are typically driven by pistons, rotary engines, or oscillating membranes. Due to the highly complex and three-dimensional geometry of the inlet duct, the difficulty of integrating such an actuator led to the design of a more simple, segmented alternative with separate locations of flow suction and injection.

The design process started with determining the proper placement of the actuators. Using results from surface pressure tests and flow visualization experiments, the locations of flow separation and vortex formation were resolved. From this information, the streamwise positions of the actuator's suction modules were strategically established for both bends of the duct. The suction slots were placed just upstream of the separation lines, where, according to a study by Kerrebrock et al., boundary layer removal is most effective in delaying or preventing flow separation[26]. Conveniently, both of these locations coincided with the junctions of inlet model sections, which allowed the fluidic actuators to be securely bolted to their adjacent, upstream duct modules. The positions of the injection slots were then governed by the physical size of the remaining fluidic actuator components and were placed as close as possible to the suction orifices.

To span the entire width of the duct and meet estimated mass flow and jet momentum needs, four actuators, placed side-by-side, were used at each bend. Lockheed Martin provided computer aided design (CAD) drawings of the duct surface

geometry that were utilized to create an actuator system that would conform to the duct shape. Using the CAD software SolidWorks, solid models of the actuator components were designed. The drawing files were then uploaded to a fused deposition modeling, rapid prototype machine. This computer controlled mechanism squirts a special, melted ABS plastic from a traversing nozzle in the shape of the part. This process is repeated for several layers, and upon cooling, a durable model results. The advantage of using this manufacturing technique is the ability to easily construct parts having complex geometries. Fine tolerances are not achievable, but the speed and low cost of this method make it ideal for research oriented projects.

Figure 13 shows a schematic of the flow control system. Fluid from the duct first enters the actuator through a 25 cm wide suction slot. Poisson-Quinton and Lepage found that the best way to control separation via boundary layer suction was through a finely perforated surface[27]. Therefore, the opening was covered by a perforated aluminum sheet. The sheeting was 0.8 mm thick and contained 1.5875 mm holes spaced 3.175 mm apart. A plenum chamber was utilized to equalize the pressure below the perforated sheet and provide an evenly distributed ingestion of the duct fluid.

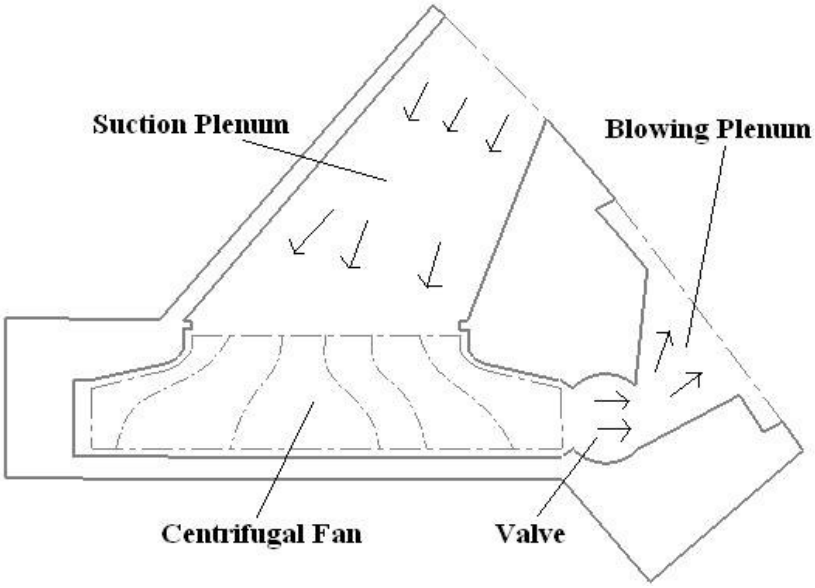

Figure 13: Schematic of the Fluidic Actuators

Below the suction chamber is the second component of the fluidic actuator, the fan compartment. Here, an enclosed centrifugal fan pulls air from the plenum and accelerates it for injection into the duct flow. The fan has an outer diameter of 67.85 mm and was originally intended for use in small, handheld vacuums. The cartoid-shaped fan housing is used to efficiently direct the flow towards the exit of this module. The fan and compartment, in a detached state from the rest of the fluidic actuator, can be viewed in Figure 14. Figure 15 presents photographs of the assembled suction plenum chambers and fan compartments for both the first and second bend actuator arrays.

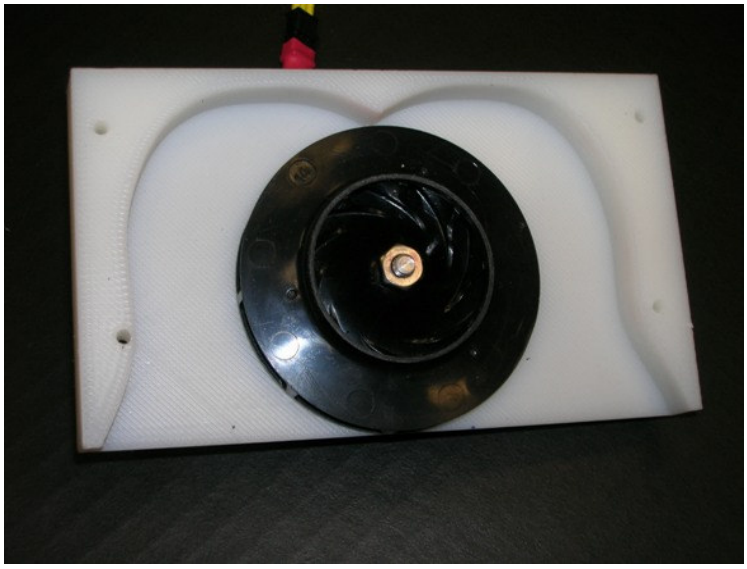

Figure 14: Centrifugal Fan and Fan Housing

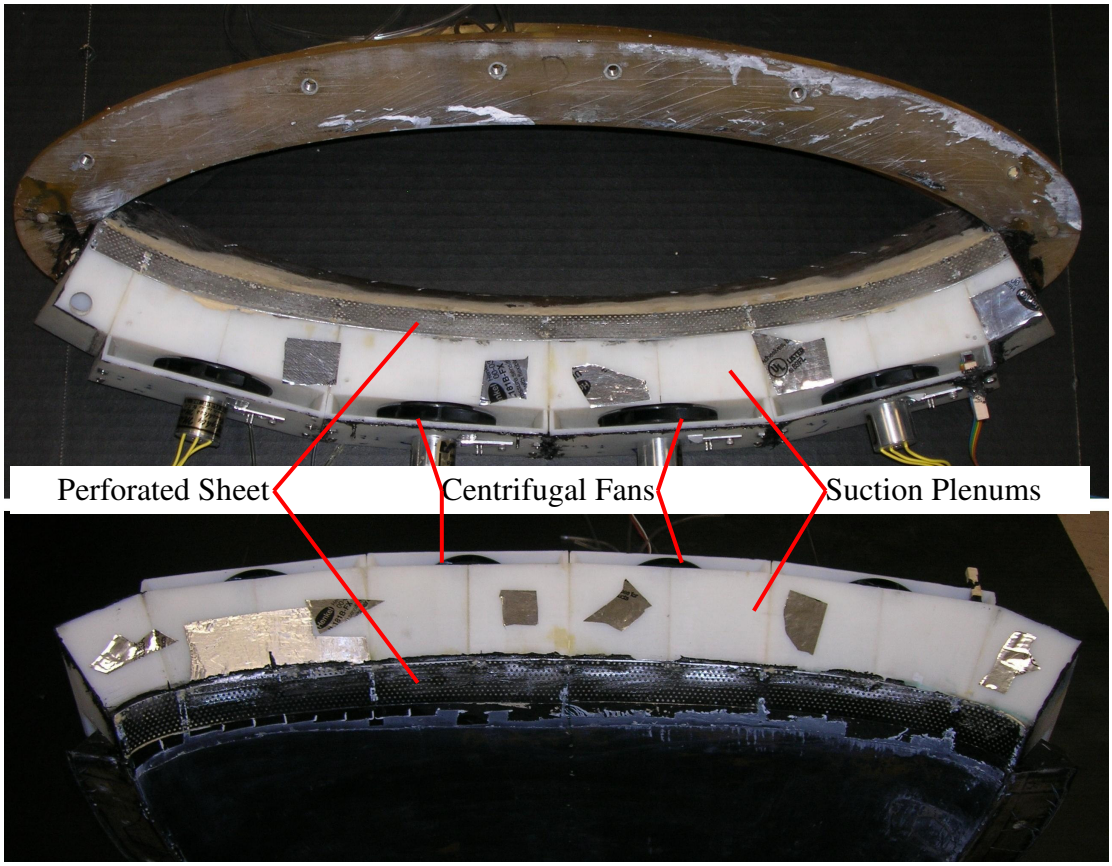

Figure 15: First and Second Bend Suction Plenum Chambers and Fan Compartments

After being energized by the fan, the fluid enters another plenum chamber through a slotted shaft. The shaft is 12.7 mm in diameter with a 6.35 mm slot. It can be rotated to become an oscillating valve for pulsed air injection, or, alternatively, remain open to produce steady blowing. During unsteady actuation, two jet pulses are produced per revolution of the shaft.

The rotating shafts of the four actuators were linked together to allow operation by a single motor. To accommodate the angular misalignment of the actuators, universal joints were employed. These couplers were guided by miniature bearings and affixed to the slotted shafts by set screws. This design aspect is demonstrated in Figure 16 by a photograph of the joined valves before their insertion into the fluidic actuator devices.

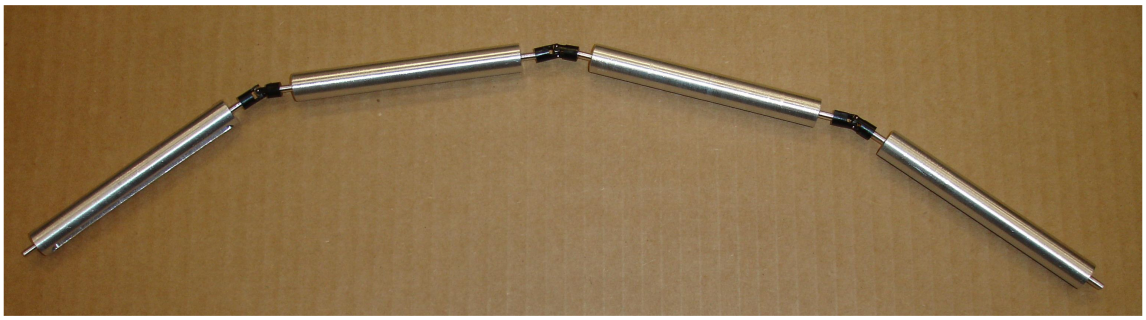

Figure 16: Slotted Shaft Valves Linked with Universal Joints

The blowing plenum, which is the third module of the fluidic actuator system, is again used to equalize the pressure before the air reenters the duct. This action ensures that the exit velocity of the created jet is common to all slots. The volume of the plenum chambers for the four separate actuators was kept constant to provide similar frequency effects across the span of the duct during pulsed blowing. A blowing plenum with an installed slotted shaft valve is shown in Figure 17.

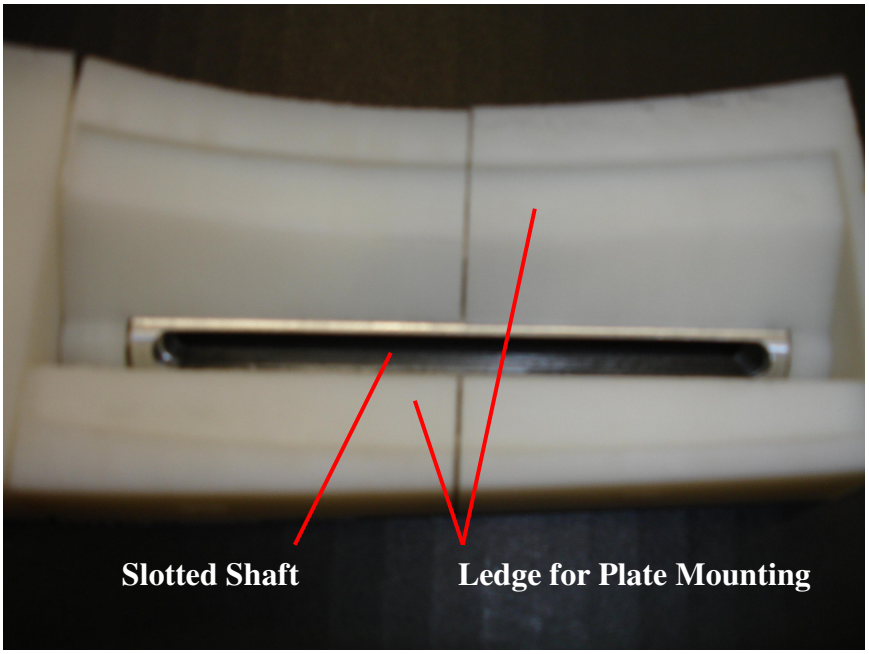

Figure 17: Slotted Shaft Valve Installed in a Blowing Plenum Chamber

Partitioning the pressurized plenum from the duct flow is a slotted plate. These plates are interchangeable to allow the exploration of several different slot sizes, shapes, orientations, and locations. The plates used for the study presented in this document feature five slots placed parallel to the streamwise direction. The slots are 1.5 mm in width by 20 mm in length and are spaced approximately 23 mm apart. To date, plates with three streamwise slots and plates with slots angled at 10 and 30 degrees to the freestream have been constructed, but were not investigated for this thesis. Figure 18 shows the entire set of blowing plenum chambers, while the complete actuator for the first bend can be seen mounted to the upstream first bend module in Figure 19.

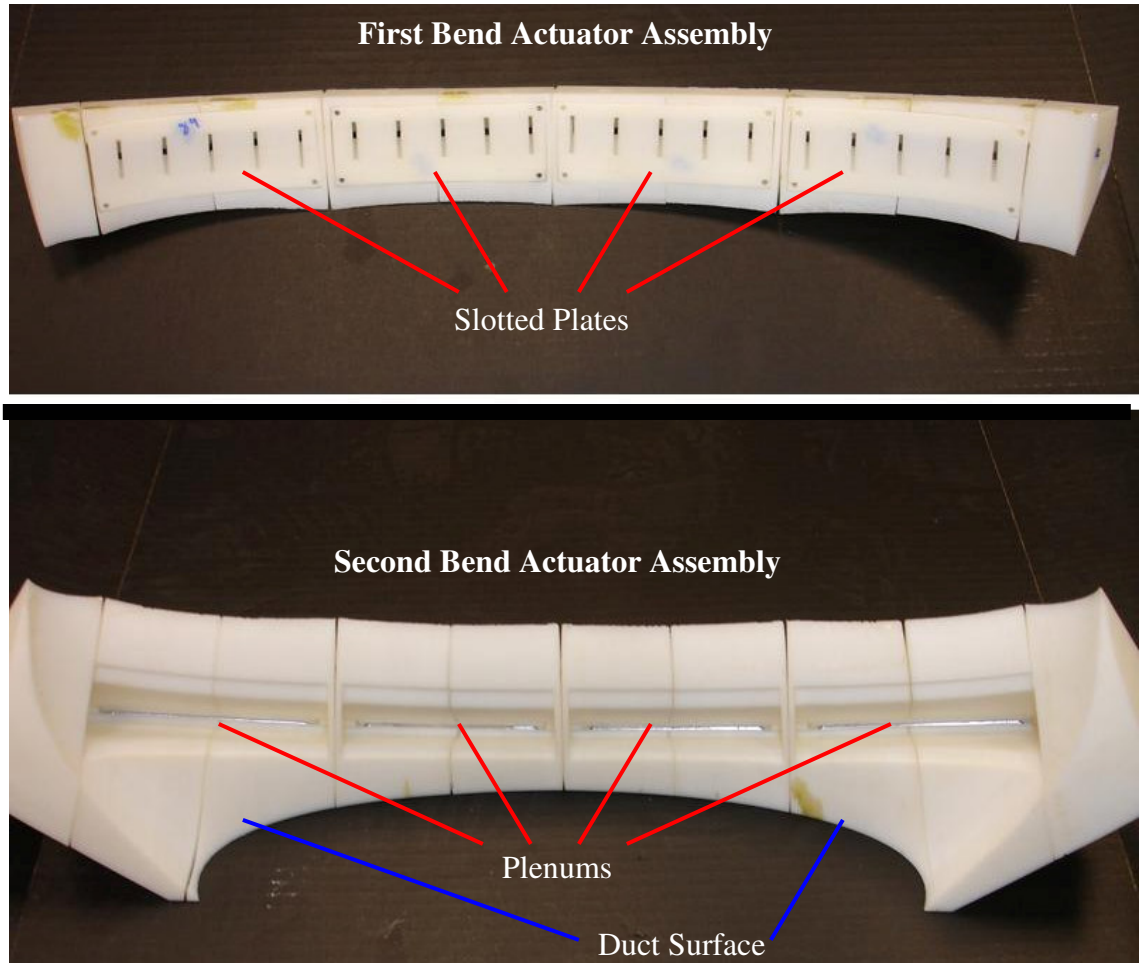

Figure 18: Assembled First and Second Bend Blowing Plenum Components

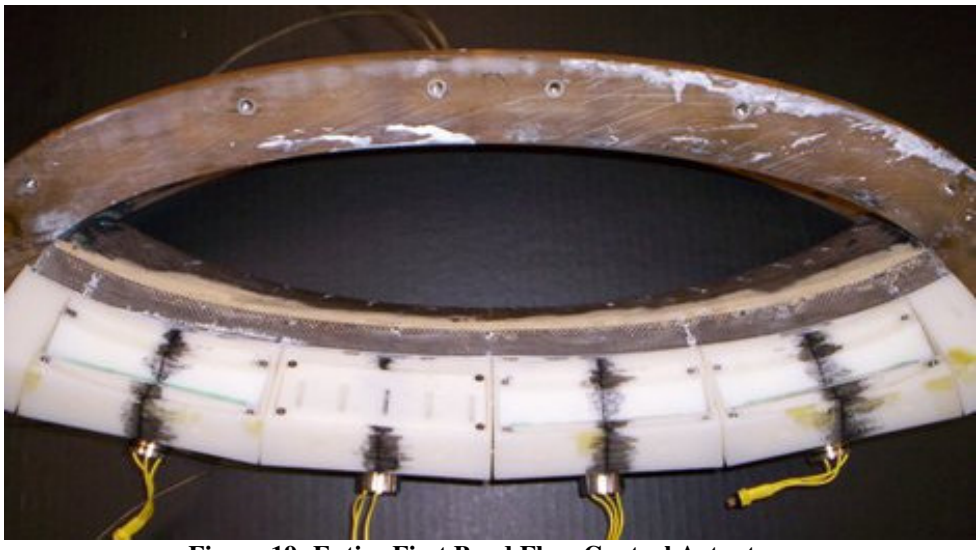

Figure 19: Entire First Bend Flow Control Actuators

Actuator Control

Traditional SJA technologies rely on a single actuator driving mechanism to provide both momentum and frequency to the fluid. In such a configuration, the jet velocity is coupled to the actuation frequency. With the fluidic actuators designed for this study, this restriction is not relevant because the fans that produce the jets can be independently adjusted. This fact could be a significant advantage in the control of the secondary flows in an axially-compact S-duct.

The centrifugal fans were powered by Mighty Micro 010 brushless motors from AstroFlight, Inc. These direct current (DC) motors, typically employed in miniature, radio-controlled (R/C) aircraft, are extremely small and lightweight. The slotted shaft assembly for each bend was rotated separately by Mighty Micro 020 brushless motors. These motors are similar to those used for the fans, but are about twice the length for the inclusion of a gearbox. This addition allows them to be utilized in applications requiring higher torque. To further increase the torque provided by the pulsor motors, additional gearing with a 2:1 ratio was employed externally. Both types of motors are presented below in Figure 20.

The ten electric motors were powered by four, 12 volt, deep cycle marine batteries. The batteries, rated at 90 amp-hours each, were connected in parallel to ensure evenly distributed power consumption and loss of charge. At maximum motor speeds, the battery system was able to sustain its charge for approximately four hours.

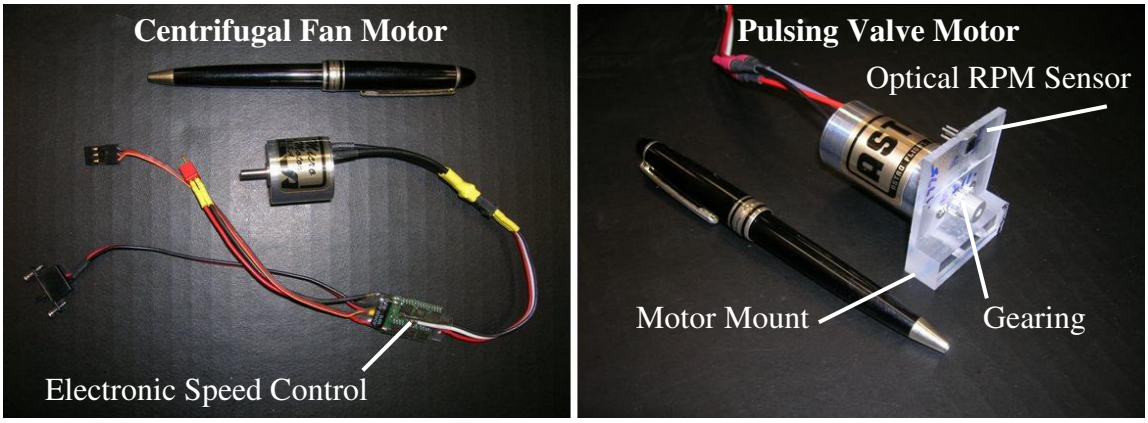

Figure 20: Electric Motors Used to Drive the Fans (Left) and Slotted Shaft Valves (Right)

Control of the motors was accomplished through electronic speed controllers provided with the Mighty Micro systems. These devices take the servo-based pulse width signal supplied by the radio receiver of an R/C product, and output the necessary current to the motor. To generate these pulse width signals, thus emulating a radio receiver, a 32-channel servo controller was obtained from Lynxmotion Robotics. This PC-based card takes serial commands as input and produces the corresponding pulse width modulation. With this support system, operation of the fluidic actuators by computer was possible.

To apply feedback control, software was created using LabVIEW. The LabVIEW program received user input in the form of fan and pulsor frequencies, then continually communicated with the Lynxmotion servo controller and RPM sensors to maintain the desired rotational rates. These optical sensors, triggered by reflective tape, reported the frequencies of the motors through two, 8-channel USB-6009 data acquisition boards from National Instruments. These external boards feature 14-bit resolution at a maximum sample rate of 48,000 samples per second and connect to the

PC via USB ports for convenience. For further clarification of the control and acquisition methods utilized in this study, Figure 21 shows a flowchart illustrating the process.

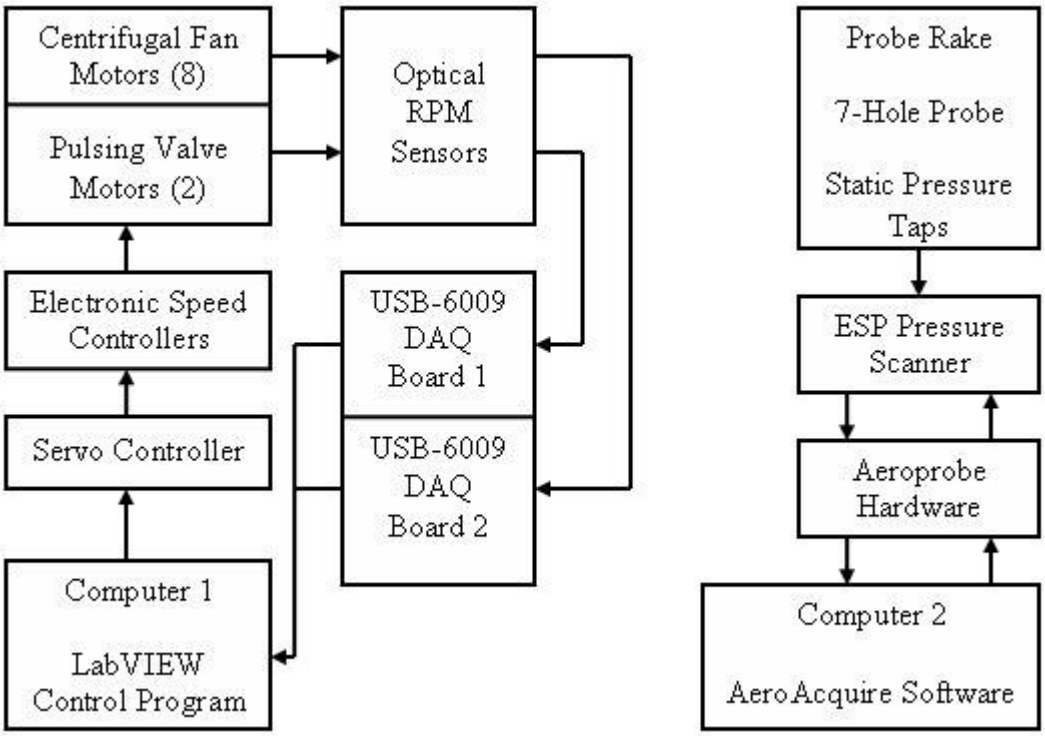

Figure 21: Schematic of the Control and Acquisition Setup

RESULTS AND DISCUSSION

This section will document the results of experiments performed on the serpentine inlet duct and the fluidic actuator devices. First, the characteristics of the actuator system will be described from the analysis of bench top tests. Then, results from the baseline, resin duct model will be shown through flow surveys at the engine face, wall static pressure distributions, CFD analysis, and flow visualization experiments. Finally, using similar methods, the effects of flow control actuators on the performance of the duct will be presented.

Bench Top Fluidic Actuator Performance

Before the actuator devices were integrated into the fiberglass duct model for testing, experiments were run to characterize their performance. Given that the actuators are driven by centrifugal fans, they are susceptible to reduced efficiency when an adverse pressure gradient is applied across them. Such is the case for their installation locations in the serpentine inlet. Due to the flow physics inside the duct, the static pressure at the suction point is lower than that at the blowing point. Therefore, for a given fan rotational speed, the velocity of the resulting jet is reduced as this pressure differential is increased.

To simulate the pressure gradient across the fan, the suction plenum of the fluidic actuator was affixed to an open-circuit wind tunnel, while the blowing plenum was exposed to ambient pressure. Several pressure differentials were attained by varying the flow speed within the wind tunnel. By affixing the five-slotted plate to the blowing

chamber and monitoring the steady jet velocity with a tiny, boundary layer probe, a series of calibration curves was produced to map the fan effectiveness at various fan speeds and pressure gradients. The boundary layer probe was connected to a Barocel transducer with an accuracy of 0.05% of reading. The static pressure in the wind tunnel was acquired from a handheld manometer with an accuracy of 0.1% of full scale. A plot showing the performance of the steady blowing jet at several pressure differentials is presented in Figure 22. It should be noted that tests were performed for all five slots of the actuator and produced nearly identical values.

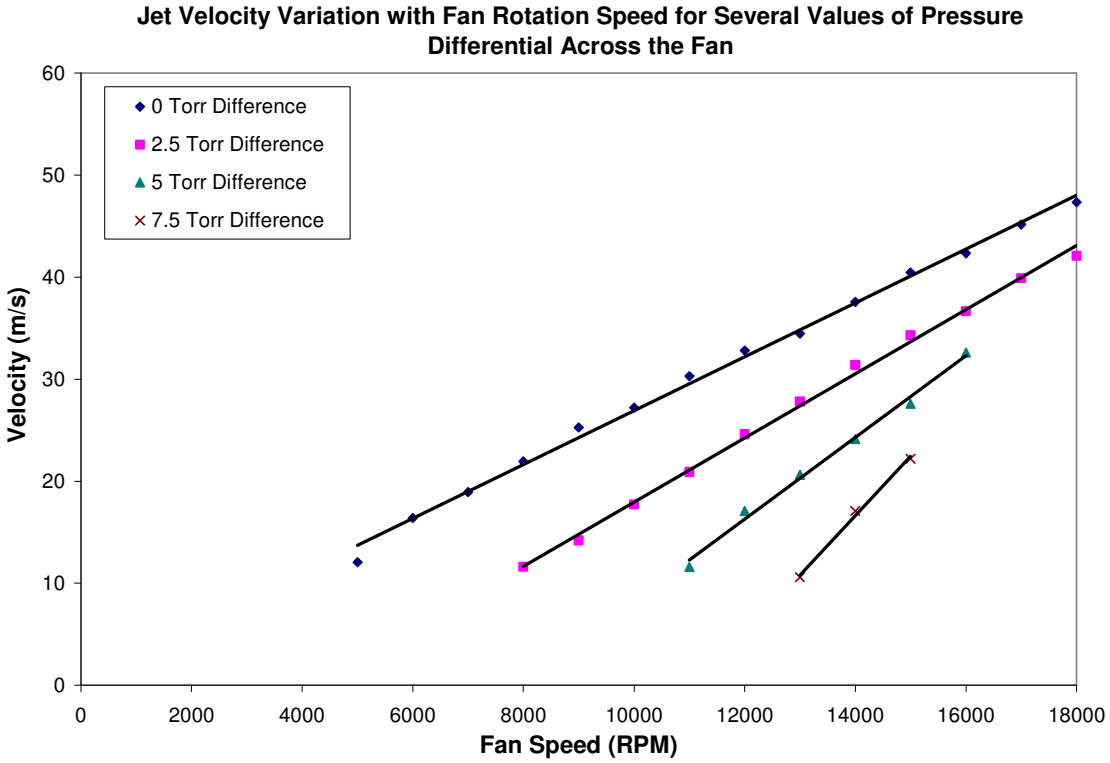

Figure 22: Steady Blowing Jet Velocity Calibration

As evident in the above plot, the relationship between fan rotational rate and the exit velocity of the jets is linear. It can be inferred from the similar slopes of the curve

fits that, for a given fan speed, the jet velocity varies linearly with pressure differential as well. This aspect of the actuators could be highly advantageous for the application of closed-loop feedback control, as a nonintrusive means of acquiring real-time jet velocities in the duct is beyond the scope of this research.

Additional bench top experiments were done to assess the operation of the fluidic actuators for pulsed injection. This investigation was performed with no pressure applied across the fan. To measure the high frequency, unsteady jet velocity, an IFA 300 hot-wire anemometry system from TSI was employed. Fan speeds of 9000 RPM, 12,000 RPM, and 15,000 RPM were each tested at frequencies of 80 Hz, 100 Hz, 200 Hz, and 400 Hz. In Figure 23, the unsteady jet velocity variation with time for a pulsing frequency of 100 Hz can be seen. A fast Fourier transform (FFT) of the 15,000 RPM plot is presented in Figure 24. The graph clearly shows that a frequency of 100 Hz is dominant.

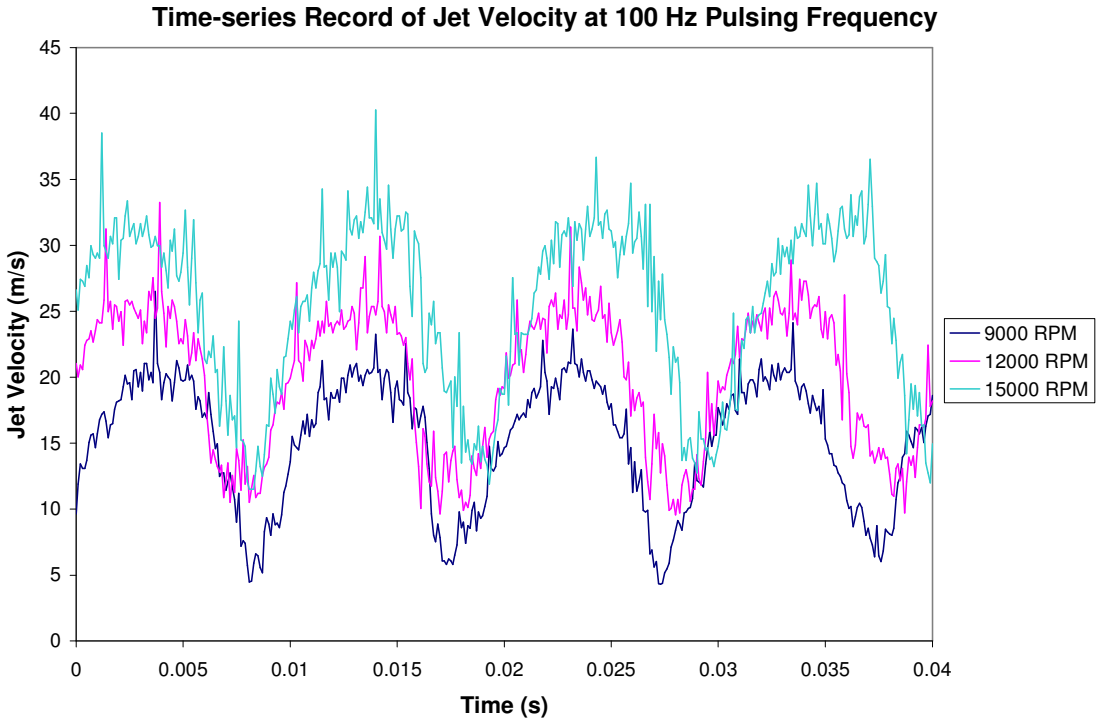

Figure 23: Unsteady Fluidic Actuator Performance

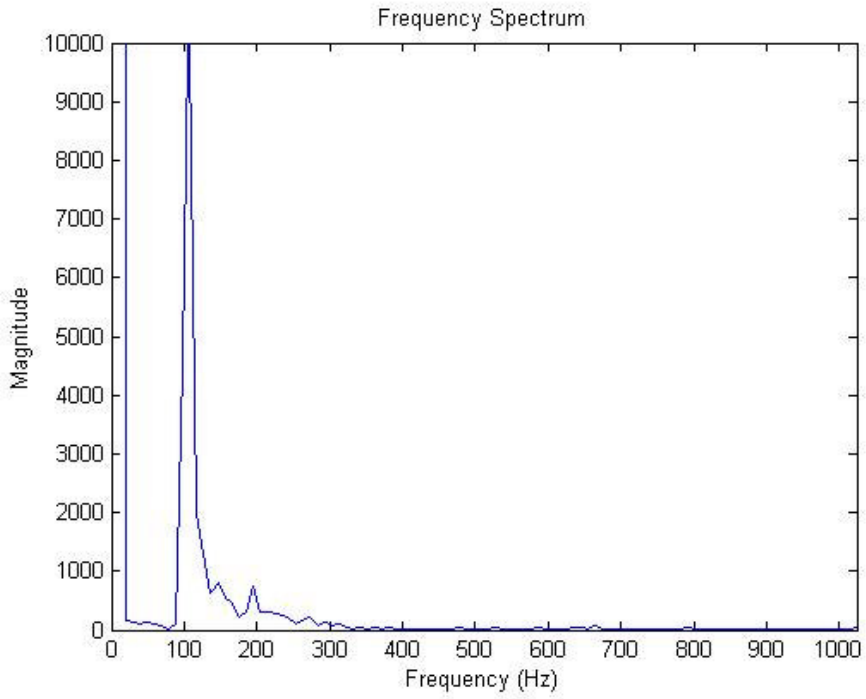

Figure 24: FFT of the Jet Velocity at a Fan Speed of 15,000 RPM and a Pulsing Frequency of 100 Hz

The oscillating jet that is produced by the flow control actuator follows a sinusoidal pattern. However, due to inertial effects of the fluid in the plenum, pressurized air remains in the chamber for a brief time after the valve is closed. Therefore, the minimum jet velocity never reaches 0 m/s. Also, the plenum and backpressure limitations of the centrifugal fan create a bias in the mean jet velocity. This characteristic is illustrated in Figure 25. The average velocity of the unsteady jet is approximately 63% of that of the steady jet for all fan speeds. Additionally, Figure 25 shows a slight decrease in mean jet velocity with increasing frequency. This trend is again caused by the inertia of the fluid. As the rotational rate of the shaft is raised, less time exists for the flow to accelerate and travel the length of the slot. Therefore, a decreased amount of energized fluid passes from the fan compartment to the blowing plenum.

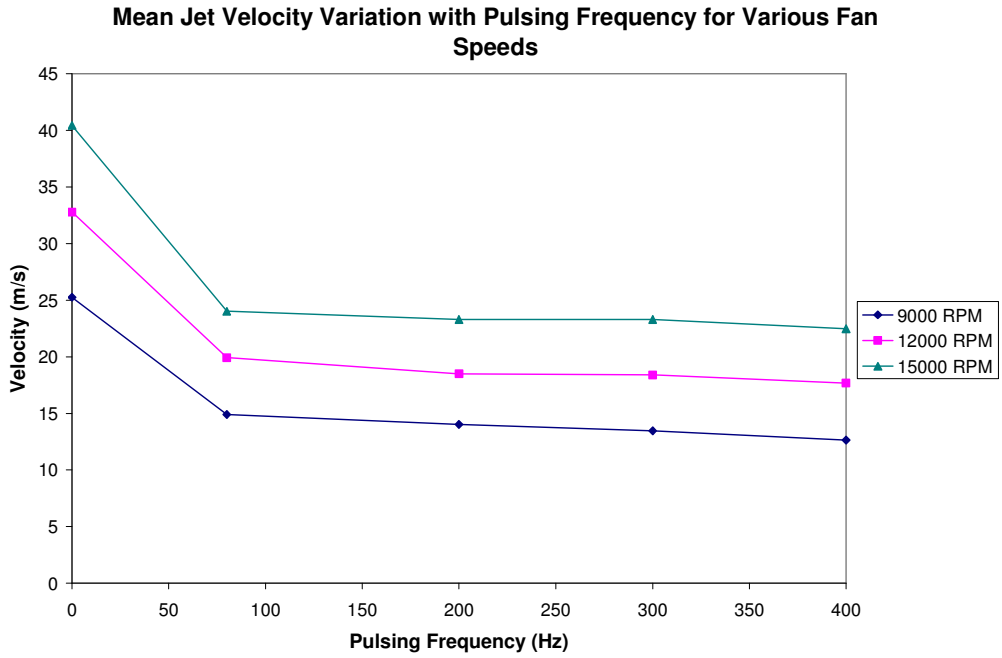

Figure 25: Average Jet Velocity of the Oscillating Actuator at Various Fan Speeds

Baseline Duct Model

Before design of the flow control actuators took place, the flow within the baseline inlet was analyzed. To accomplish this task, several experiments were performed using the resin duct model from Lockheed Martin. These tests provided a great deal of insight into the formation of the secondary flows within the compact, serpentine inlet. By combining the results of this investigation with the knowledge obtained from literature on the subject, a keen understanding of the flow physics was acquired.

CFD Analysis

In addition to physical surveys of the flow, computational methods were also employed to gain an understanding of the flow phenomena. The advantage of CFD is the multitude of options available in post-processing. One can view velocity, total or static pressure, vorticity, and many other important aerodynamic quantities at any location in the flowfield. Also, streamlines can be plotted to reveal information regarding the fluid mechanics. However, the downside of computationally exploring such a complex flowfield is the accuracy of the results. As shown by Hamstra et al.[1], CFD solutions for the flow in this duct fail to capture the extent of flow separation, vortex size, and pressure loss. Nonetheless, computational analysis does show significant secondary flow development. Therefore, its use as a basis for qualitative exploration of the flow physics is justified.

For the CFD analysis performed in this study, a three-dimensional, unstructured Navier-Stokes solver with k-omega turbulence modeling was utilized. This code, named

UNS3D, was written by a Ph.D. student in the Aerospace Engineering Department at Texas A&M University. A mesh of approximately 400,000 nodes was created using an in-house code as well. Plots of the results, shown below, were produced in Tecplot. Figure 26 shows the total pressure contours at several axial locations, while Figure 27 displays a group of streamlines, colored by Mach number, that reveal the second bend vortex formation.

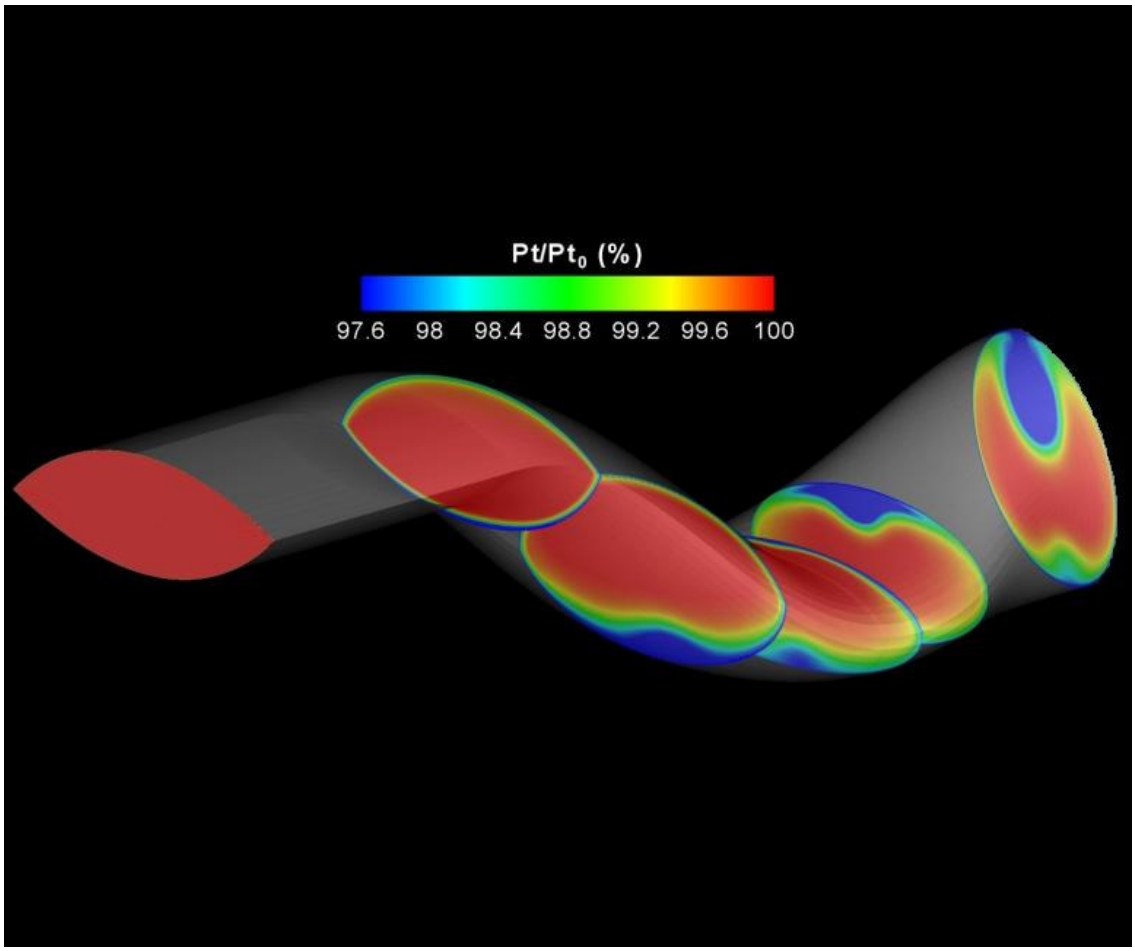

Figure 26: Pressure Contours within the Duct Resulting from CFD Analysis

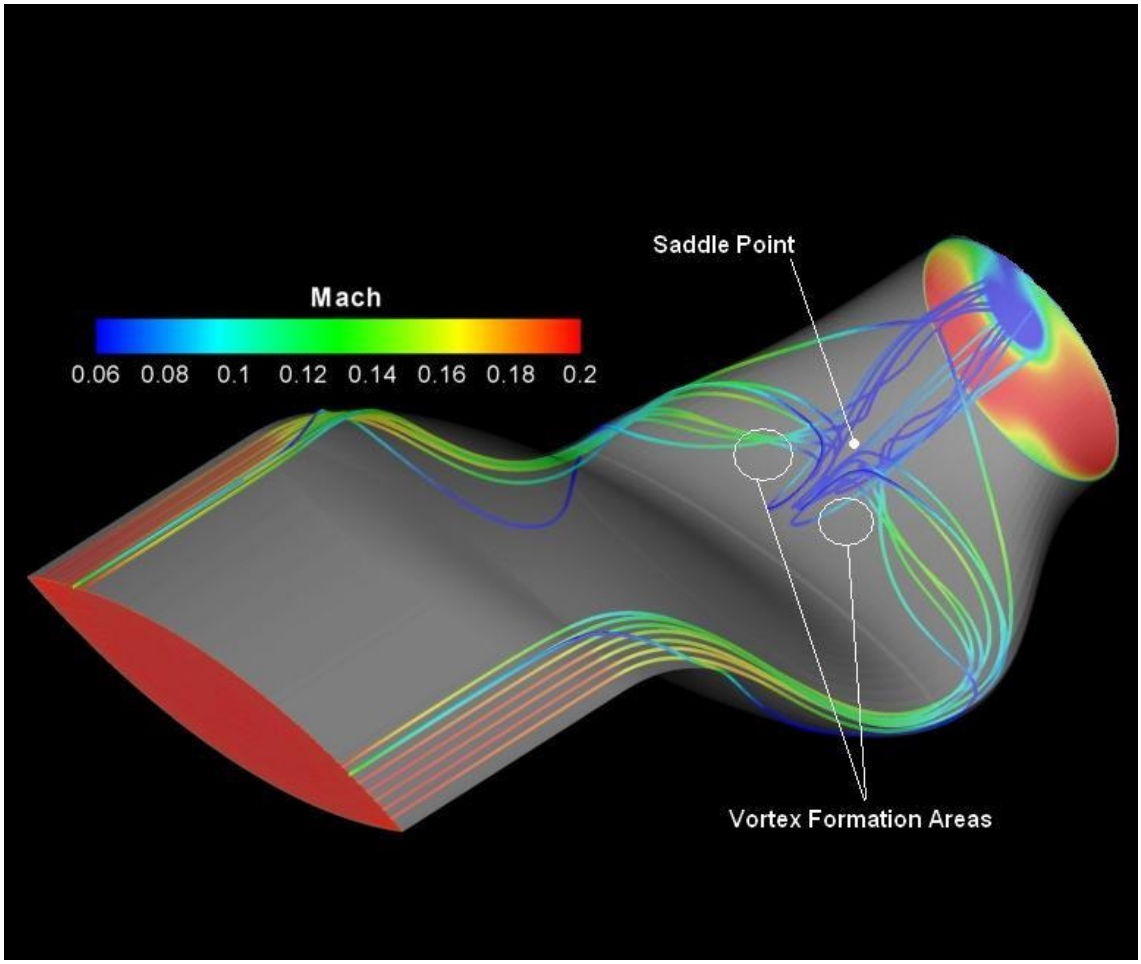

Figure 27: CFD Streamline Trace

Combining the information revealed by each of these plots, the description of the secondary flow development provided in the introductory section of this document is confirmed. Just downstream of each bend, flow separation causes the emergence of low pressure regions near the wall that are concentrated towards the center of the duct (signified by the blue areas). These pressure deficits cause the flow to rush in from the sides of the duct, converging at the centerline where the fluid is then forced into a vortical pattern.

Surface Flow Visualization

For a further qualitative study of the mechanisms governing the secondary flow formation, flow visualization on the walls of the duct was carried out. To accomplish this test, a mixture of titanium dioxide, kerosene, mineral oil, and oleic acid was employed. The titanium dioxide, a heavy, white powder, becomes suspended in the compound. The concoction can then be painted onto the surface. When the flow is activated, shear stresses at the wall force the liquid components of the mixture to migrate downstream, leaving behind the tiny particles of titanium dioxide. In Figure 28 and Figure 29, photographs of the first and second bends of the duct, respectively, are shown after undergoing an application of the titanium dioxide compound. The viewpoint of the first bend picture is upstream, looking at the bottom wall. In the second bend photograph, the top wall is the focus from a downstream location. In both pictures, the merging near-wall flow is evident, as are the locations of vortex lift-off. In the photograph of the first bend flow visualization, a line indicating the point of flow separation can be seen. A comparison of the two bends indicates that the second bend vortices are much stronger than those of the first bend. This is evident from the thick pooling of liquid at the first bend vortex cores, where too little flow energy existed to pull the mixture off the duct surface.

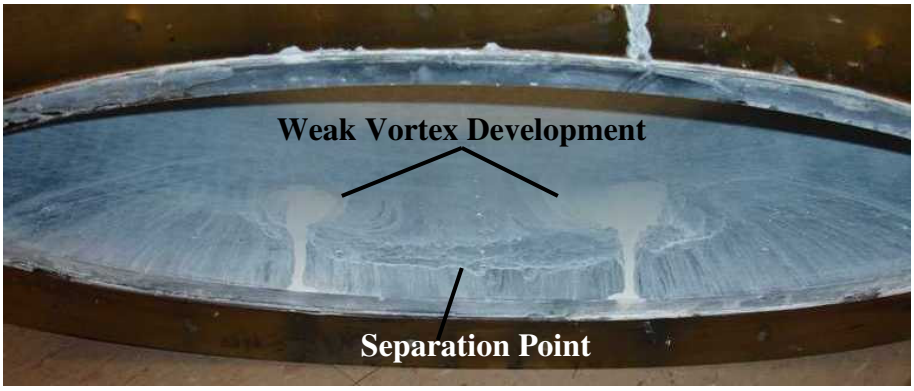

Figure 28: First Bend Surface Flow Visualization

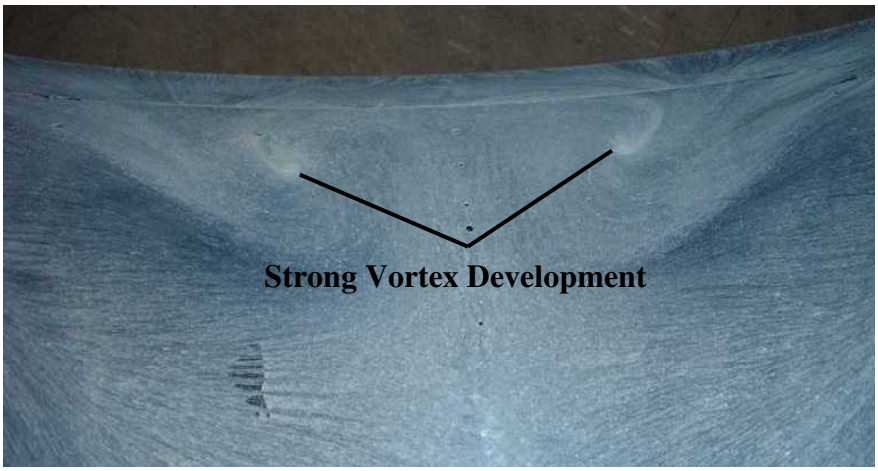

Figure 29: Second Bend Surface Flow Visualization

Surface Static Pressure Taps

Quantifying the formation of secondary flows in this S-duct began with an experiment involving surface static pressures. Using the data presented in Figure 30, regions of accelerating and decelerating flow were identified, as were areas of flow separation. Both the bottom and top surfaces are represented in the static pressure plot of Figure 30. For spatial reference, the duct geometry is included as the background image of the graph. These static tap tests were run at an inlet Mach number of 0.18 with

a Reynolds number of 1.03 x 10^6. In the plot below, P_{ref} is the total pressure measured by the Pitot tube located in the second entrance module of the duct.

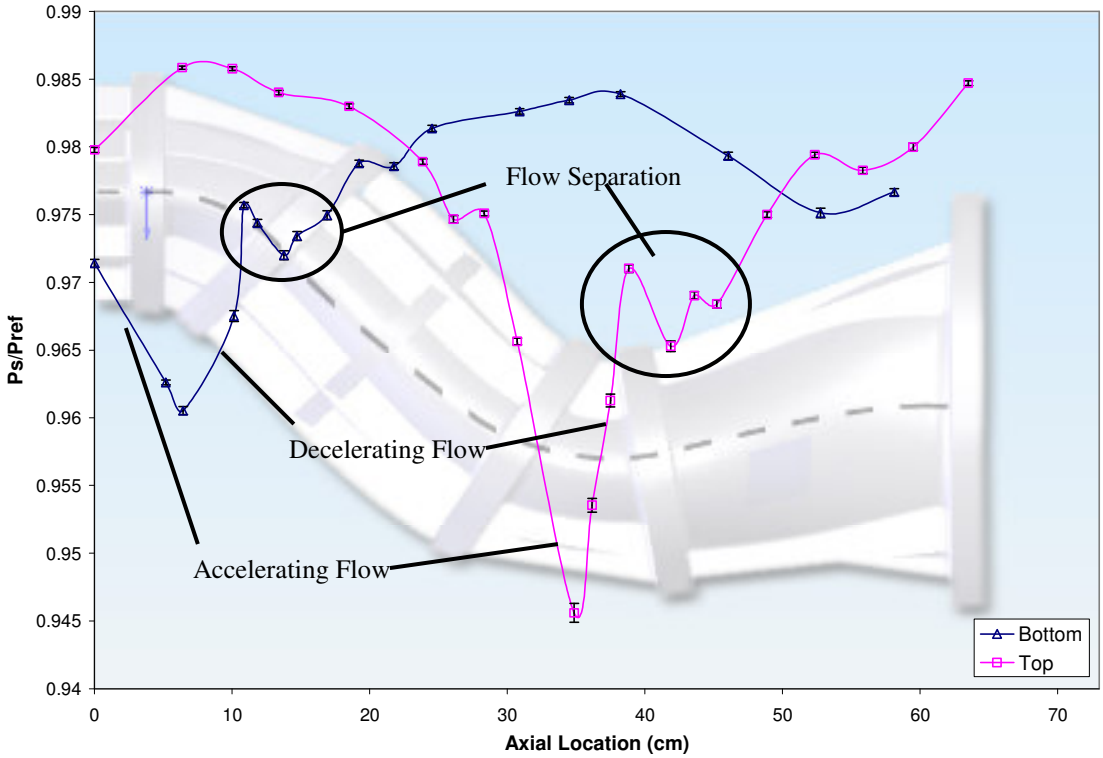

Figure 30: Wall Static Pressure Distribution of the Baseline Duct Model

Engine Face Survey

The aforementioned seven-hole probe was used to obtain a detailed view of the pressure and velocity distributions at the engine face plane of the baseline serpentine inlet. The data acquired with the probe was instrumental in characterizing the final nature of the secondary flows. Figure 31 presents these results in the form of a contour plot of the pressure loss coefficients calculated at each of the points. Superimposed over the contours is a plot of the transverse velocity vector field.

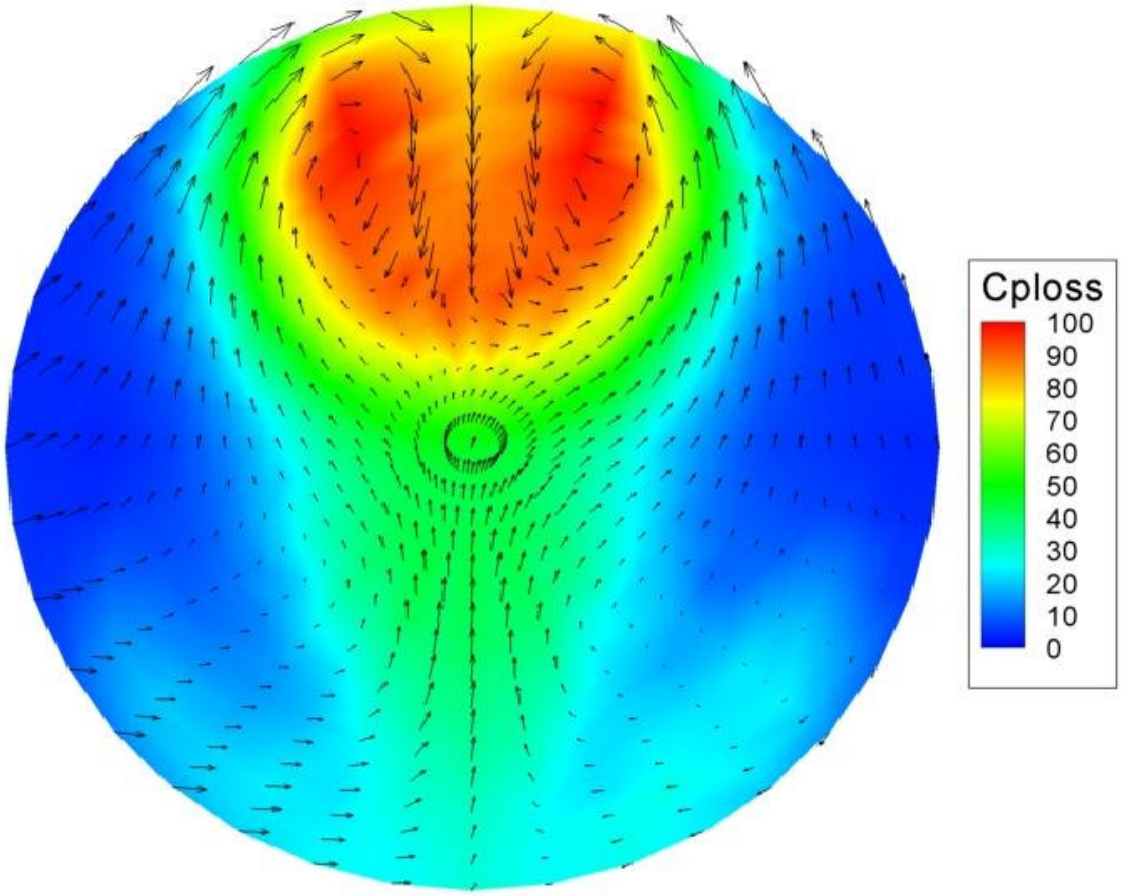

Figure 31: Engine Face Total Pressure Loss Coefficient Contour Plot with Velocity Vectors

As clearly shown in Figure 31, the strong, counter-rotating vortices shed from the second bend constitute the dominant flow features that deteriorate the performance of this S-duct. Therefore, flow control efforts will focus on weakening or eliminating these structures to improve inlet efficiency. The vortices, denoted by the red region at the top of the plot, cover nearly an eighth of the engine face area and create a region of severe pressure deficit.

Close inspection of the above plot does not show any indication of the presence of vortices produced by the first bend. A low pressure strip does extend to the bottom

wall of the duct, but the vectors do not reveal any significant circulation. At this stage in the research project, the evolution of the vortices produced by the first bend fluid dynamics is unclear. One possibility is that they feed into the second bend vortices and are consumed. Another is that, due to their weak nature, the vortices break down after diffusing over the lower portion of the duct. Future efforts at Texas A&M University will employ CFD and experimental techniques in an attempt to clarify this occurrence.

Flow Control – Suction

Initial flow control attempts were conducted by applying only suction to the bends of the serpentine inlet. The goal of this method was to delay or prevent separation to increase the pressure recovery at the engine face plane. From the explanation of vorticity signature provided in the Introduction section of this thesis, it was expected that suction would not be successful in deterring the development of the secondary flows. However, an investigation into the effects of this control technique on the severity of the pressure loss within the secondary flow structures was of interest.

Boundary layer suction is the process of removing low energy fluid that is prone to separation when exposed to adverse pressure gradients and deflecting higher energy flow towards the wall[28]. To achieve this action within the duct, the fluidic actuator system, minus the blowing plenum components, was integrated into the model. In this configuration, the low pressure side of the centrifugal fans was exposed to the static pressure in the inlet while the high side was connected to vacuum pumps. The vacuums were used to equalize the pressure across the fans to ensure their ability to remove the boundary layer flow despite the low static pressure inside the duct.

To analyze the effects of suction on the performance of the jet engine inlet, surface static pressure and engine face surveys were again run at a Mach number of 0.18. Three levels of suction, expressed as a percentage of the core mass flow, were explored. The mass flows were measured with probes located in the vacuum pump hosing. Figure 32 shows the change in static pressure for the top and bottom surfaces of the duct when suction amounts of 1.25%, 1.75%, and 2.25% were applied. In the plot, the wall static pressures for each case follow a similar distribution, but are shifted. The vertical shift represents a decrease in total pressure loss and the horizontal displacement indicates a delay in flow separation. The static pressure tests showed that first bend flow separation was delayed nearly 5 cm and the second bend separation point was moved downstream approximately 2 cm when 1.25% boundary layer suction was initiated. Increasing the amount of suction beyond 1.25% did not have any additional effect on the location of the separation point.

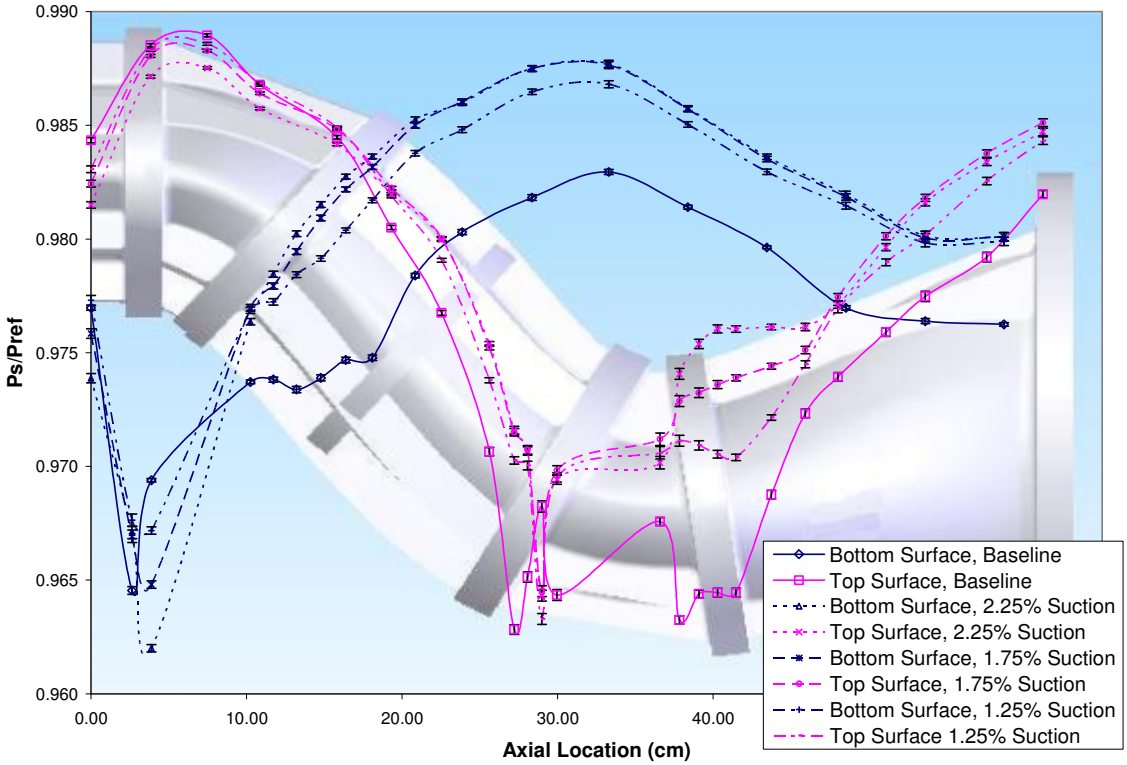

Figure 32: Comparison of Baseline and Suction Flow Control Wall Static Pressures

A seven-hole probe was again utilized to map the contours of C_{Ploss} at the engine face plane for the suction experiments. As expected, the strong vortices emerging from the second bend were still prevalent. However, with suction applied the degree of pressure recovery in these vortices and throughout the engine face was greatly increased. Also, a strong relationship developed between the amount of suction and the associated pressure loss. Each increase in suction led to a further reduction in $C_{Ploss,avg}$. This effect can be inferred from Figure 33, which shows the engine face contours of C_{Ploss} for the three values of suction. Each of the plots only portrays one half of the engine face plane with suction applied. For reference, the other half is replaced by the baseline pressure contour plot. Following the figure, Table 1 presents the values of $C_{Ploss,avg}$ and DC_{60}

obtained at the three levels of suction. The values in the table confirm that flow control by suction alone improves pressure recovery, but has little effect on flow distortion.

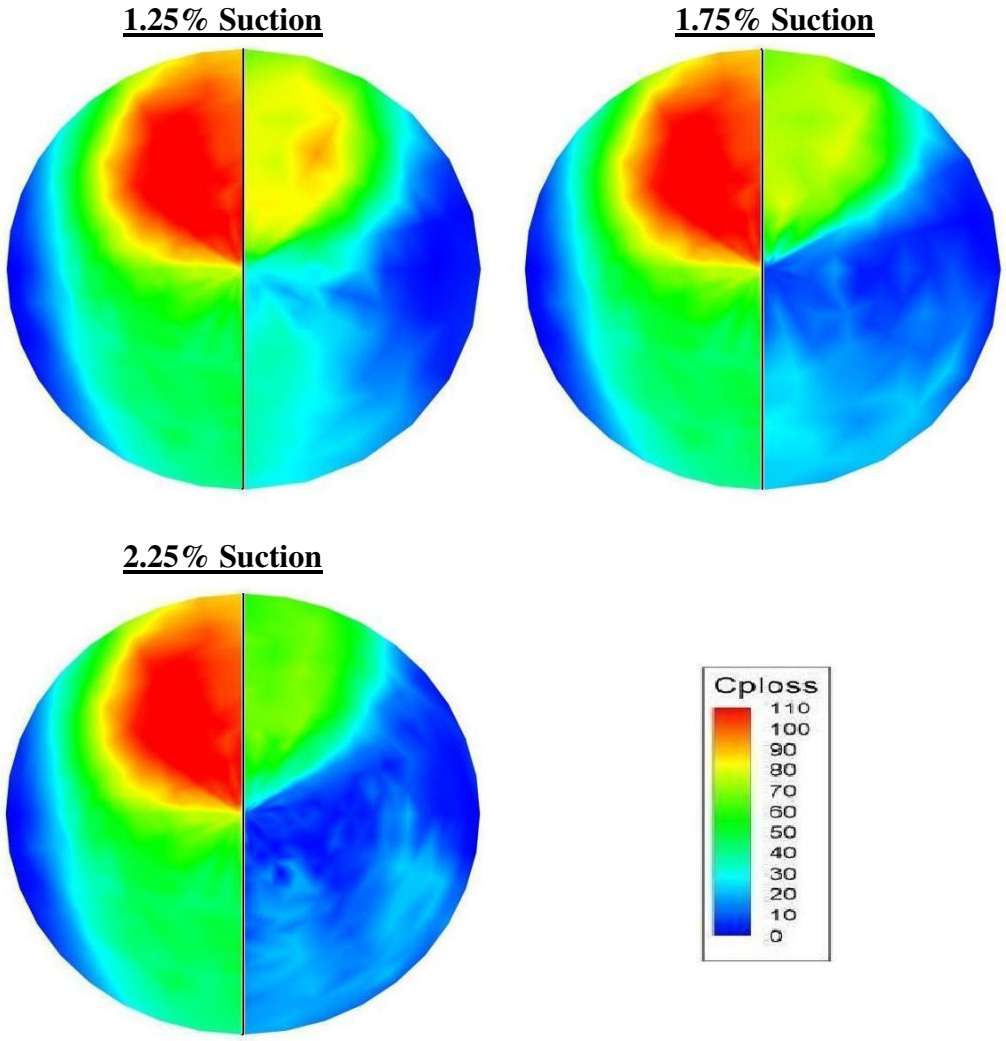

Figure 33: Pressure Loss Coefficient Contour Plots Comparing Various Amounts of Suction Flow Control (Right Half) to the No Control Case (Left Half)

Table 1: Average Coefficient of Pressure Loss and Distortion Descriptor Values Obtained with Suction Flow Control

Suction (Mass Flow Percentage)	$C_{Ploss,avg}$	DC_{60}
0.0	66.68 ± 1.28	88.54 ± 3.66
1.25	35.44 ± 0.81	79.38 ± 3.18
1.75	24.39 ± 0.61	74.51 ± 3.13
2.25	19.82 ± 0.54	72.16 ± 3.10

Flow Control – Suction and Steady Blowing

Upon completion of the suction flow control tests, the blowing plenum chambers were reconnected to the fluidic actuator system and incorporated into the duct model. Differential pressure sensors with an accuracy of 0.009 torr were employed to monitor the real-time pressure gradient across the fans. These values were averaged over the duration of the testing and applied to the curve fits of the fluidic actuator performance plot to calculate the jet velocities. For this document, experiments with the operation of flow control via steady suction and blowing were run at an inlet Mach number of 0.09 and a Reynolds number of 5.07 x 10^5. This low velocity was chosen because the pressure differential across the fans was negligible, thus yielding the maximum efficiency of the actuators for each fan speed.

Unlike the suction case, the degree of flow control applied to the inlet by steady or unsteady injection can not be expressed only as a percentage of the core mass flow. Instead, a new term representing the momentum addition provided by the jets must be introduced because momentum injection, not mass addition, governs flow control effectiveness[28]. The parameter, called the jet momentum coefficient and denoted by C_μ, compares the momentum of the jet emerging from the slot to the momentum of the freestream fluid. The definition of C_μ used in this study was derived from the research of Amitay et al[22]. Equation 5 presents this definition for the jet momentum of the entire actuator array.

$$C_\mu = \frac{\left(\rho \cdot U^2 \cdot l \cdot w \cdot n\right)_{jet}}{\left(\rho \cdot U^2 \cdot A\right)_{duct}} \tag{5}$$

In the above equation, ρ_{jet} and ρ_{duct} are the densities of the fluid in the jet and duct core flow, respectively, U_{jet} is the exit velocity of the jet, U_{duct} is the velocity of the duct flow at the location of the actuator, l_{jet} and w_{jet} are the length and width of the slots, n_{jet} is the total number of slots for each actuator assembly, and A_{duct} is the area of the duct at the location of flow control.

Many factors contribute to the error in the value of C_μ. The primary source of uncertainty arises from the linear curve fits of the jet velocity calibration. Also, the uncertainty in the pressure measurement across the fans and the error in the velocities obtained in the bench top jet calibration must be considered. Using the constant odds approach for uncertainty propagation discussed earlier, the error in the jet momentum coefficient was calculated to be approximately 5%.

Operation of the fluidic actuators at five values of C_μ was performed to explore the effect of jet momentum on the control authority of the complex duct flows. The 32-port probe rake was employed to acquire total pressures at the engine face for plotting and for the calculation of $C_{Ploss,avg}$ and DC_{60}. Table 2 shows a summary of the results of this investigation. In Figure 34, contour plots of the pressure loss coefficient over the area of the engine face are presented.

Table 2: Effects of Steady Blowing Flow Control on the Duct Performance Descriptors

Fan Speed (RPM)	Jet Velocity (m/s)	C_μ	Mass Flow	$C_{Ploss,avg}$	DC_{60}
0	0.0	0.0	0.0 %	43.95 ± 0.84	90.69 ± 3.75
5000	13.5	0.0029	0.63 %	41.30 ± 1.23	93.08 ± 3.91
7500	20.0	0.0063	0.94 %	39.02 ± 1.17	96.92 ± 4.00
10000	26.5	0.011	1.24 %	29.66 ± 0.95	65.76 ± 2.63
12500	33.0	0.017	1.54 %	28.00 ± 0.90	53.43 ± 2.42
15000	39.5	0.024	1.85 %	27.63 ± 0.89	56.44 ± 2.59

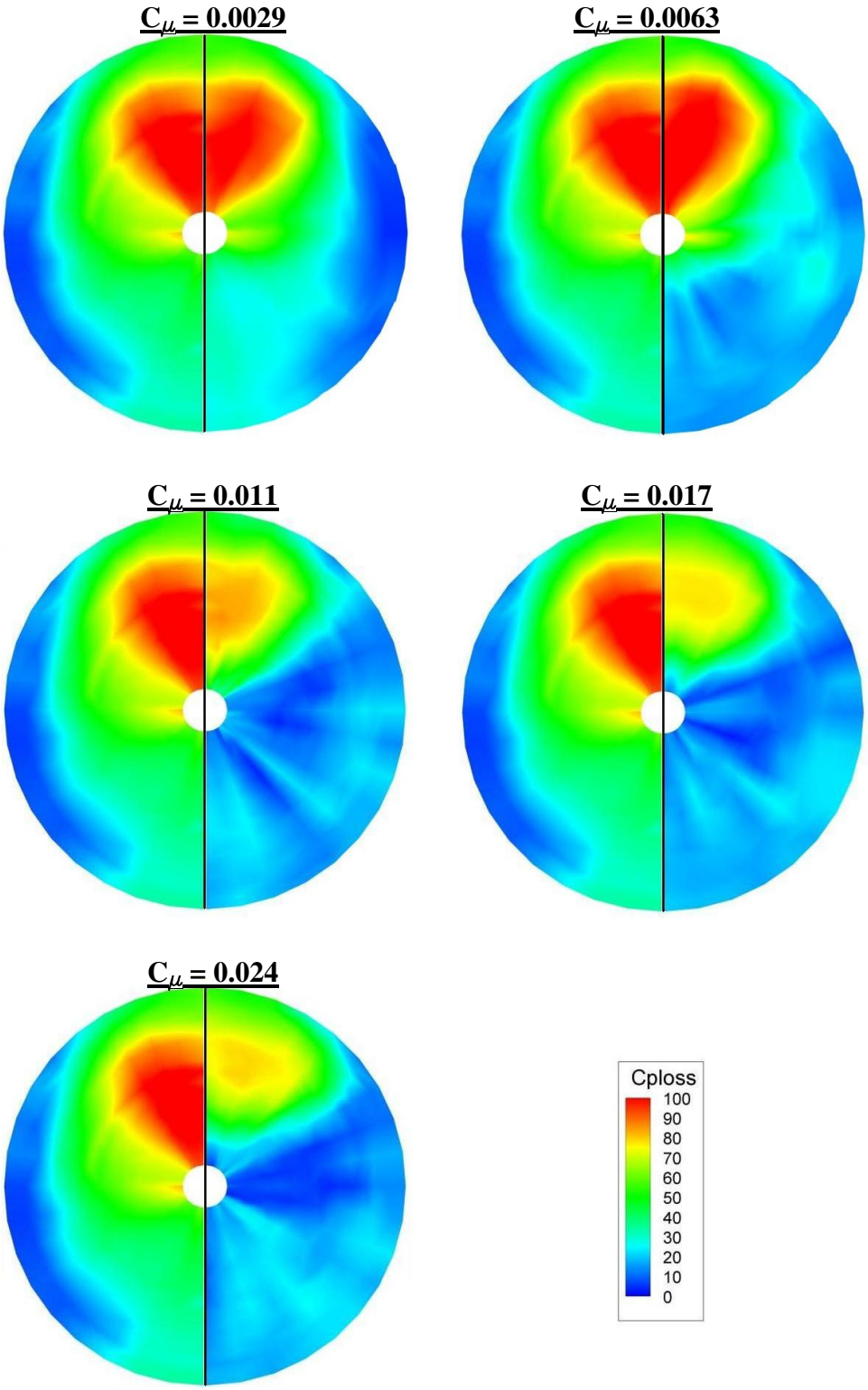

Figure 34: Pressure Loss Coefficient Contour Plots Comparing Various Amounts of Steady Injection (Right Half) to the No Control Case (Left Half)

No significant change over the baseline duct was observed for momentum coefficient values of 0.0029 and 0.0063. However, raising the application of steady injection to a C_μ of 0.011 reduced the area-averaged total pressure loss coefficient by nearly 33%. Increasing the jet momentum beyond this amount only slightly decreased the pressure loss further. Additionally, steady blowing at a C_μ of 0.011 improved DC_{60} by approximately 28%. The gains in the distortion parameter continued as fan speed was raised, but peaked at a jet momentum coefficient of 0.017 and began to worsen slightly. These aspects are illustrated in Figure 35, which shows a plot of $C_{Ploss,avg}$ and DC_{60} for flow control by both steady injection and suction alone.

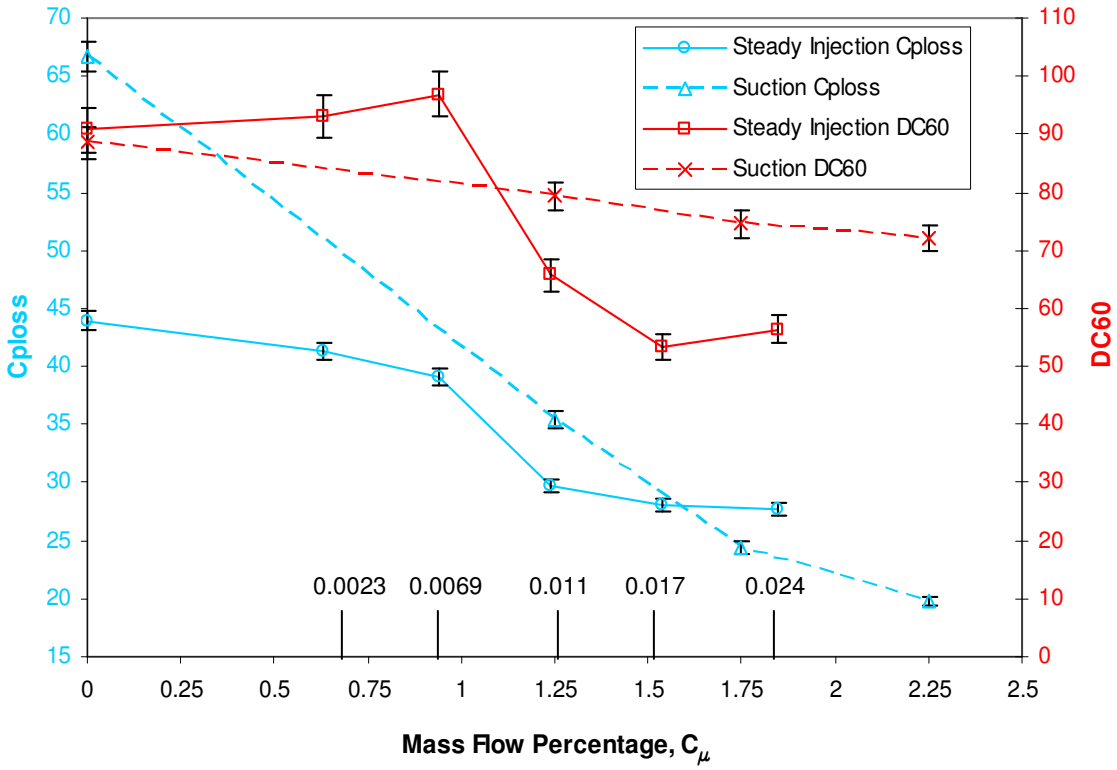

Figure 35: A Plot of the Duct Performance Parameters for Different Methods and Levels of Control

An unexpected result of the flow control techniques can be seen in the above plot by comparing the effectiveness of only suction to that of combined suction and steady blowing. Suction flow control was less beneficial than suction and injection at low levels of authority. However, as actuator mass flow was increased, the improvements in pressure recovery seen by only suction surpassed those of steady suction and blowing. At this time, the flow mechanisms behind such an outcome are not known, but one explanation involves the inconsistencies that exist between the fiberglass duct model used for the suction tests and the model employed for the suction and blowing experiments.

The information in Table 2 and Figure 35 shows that by using the fluidic actuators to produce steady jets, the generally accepted maximum value for DC_{60} of 20% was not attained. However, the improvements achieved are promising. With further optimization of the actuator systems, it is likely that goals for $C_{Ploss,avg}$ and DC_{60} will be met. The concluding section of this document will explain future attempts to optimize the actuator performance in an effort to improve the duct flowfield and reach the 20% mark.

Due to issues regarding the heating of the fan motors and the discharge of battery power, the time consuming seven-hole probe test was done for only one case of the steady injection flow control. The value of C_{μ} utilized for this test was 0.017. The contour plot of C_{Ploss} with velocity vectors for this experiment can be seen in Figure 36. The figure shows that the second bend vortices are weakened, causing them to become smaller and shift closer to the wall. It appears as though the secondary flow structures

are beginning to be spread around the duct periphery as intended, but more efficient flow control is needed to complete the process.

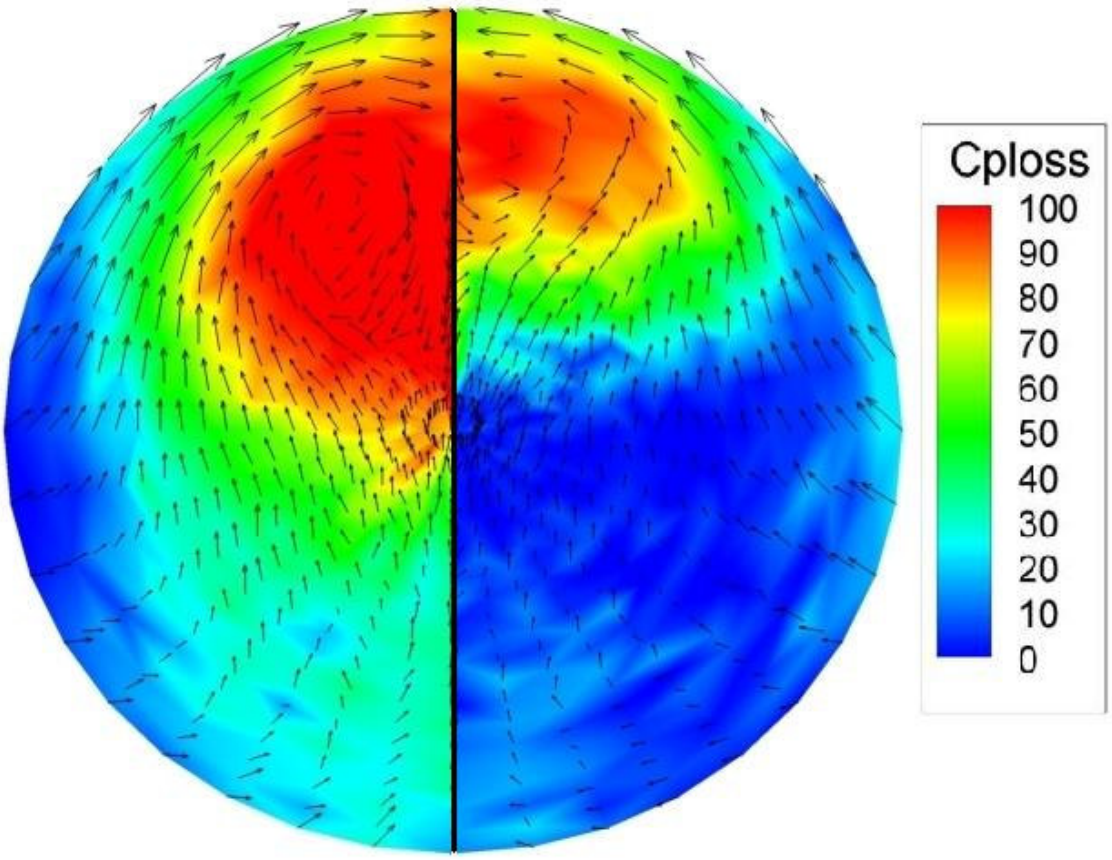

Figure 36: C_{Ploss} and Velocity Vectors of the Duct with No Control (Left Half) and with Steady Suction and Injection (Right Half)

Flow Control – Suction and Pulsed Blowing

The final technique of flow control investigated to improve the performance of the jet engine inlet involved pulsed injection through the jet slots. This method has been shown in much of the literature to be very efficient because it takes advantage of the natural frequencies related to vortex shedding from the regions of flow separation[18,19,20,28]. Therefore, less jet momentum is typically required.

In all of these studies, the most important parameter to the application of oscillatory blowing was the reduced frequency, or F^+. The reduced frequency is defined in its most generic form in Equation 6.

$$F^+ = \frac{f}{f_n} \tag{6}$$

Here, f is the actuation frequency and f_n is some natural frequency of the flow. For flow over an airfoil, Gillaranz et al.[19] showed that F^+ was coupled with x_{te}/U_∞, where x_{te} is the distance from the actuator to the trailing edge of the airfoil and U_∞ is the freestream velocity. In a more applicable statement, Mittal et al. explained that for a flow that separates and then reattaches to a surface, Equation 7 is a better means of calculating the F^+ number[29].

$$F^+ = f\frac{L_{sep}}{U_\infty} \tag{7}$$

L_{sep} is defined as the length from the separation point to the center of the recirculation bubble, and f and U_∞ are once again the pulsing frequency and freestream velocity, respectively. According to Mittal et al., values of F^+ ranging from 0.75 to 2.0 have proven successful when using the definition in Equation 7.

For the serpentine inlet employed in this research, L_{sep} can be estimated from CFD and the baseline static tap and flow visualization tests to be 0.3 m. Therefore, for the test velocity of 30 m/s, f_n is 100 Hz and pulsing frequencies of 75 Hz to 200 Hz correspond to the F^+ values of 0.75 and 2.0 stated above. However, due to the uncertainty of the L_{sep} estimation and the extremely complex flow physics in the duct, high frequency response sensors were used to verify the natural frequency. The data

acquired from the sensors was fed into an FFT code written in Matlab to produce the plot in Figure 37. The plot reveals a dominant frequency of 72 Hz, which was common to most of the points explored in the survey. It is unclear whether this frequency was the result of a flow process too complicated for Equation 7 to predict, or if the value of L_{sep} was miscalculated. Nonetheless, pulsing frequencies of 75 Hz, 100 Hz, 125 Hz, and 150 Hz were chosen to explore reduced frequencies on the order of both values of the natural frequency. In the remainder of this document, the natural frequency used to calculate F^+ will be the experimentally acquired frequency of 72 Hz.

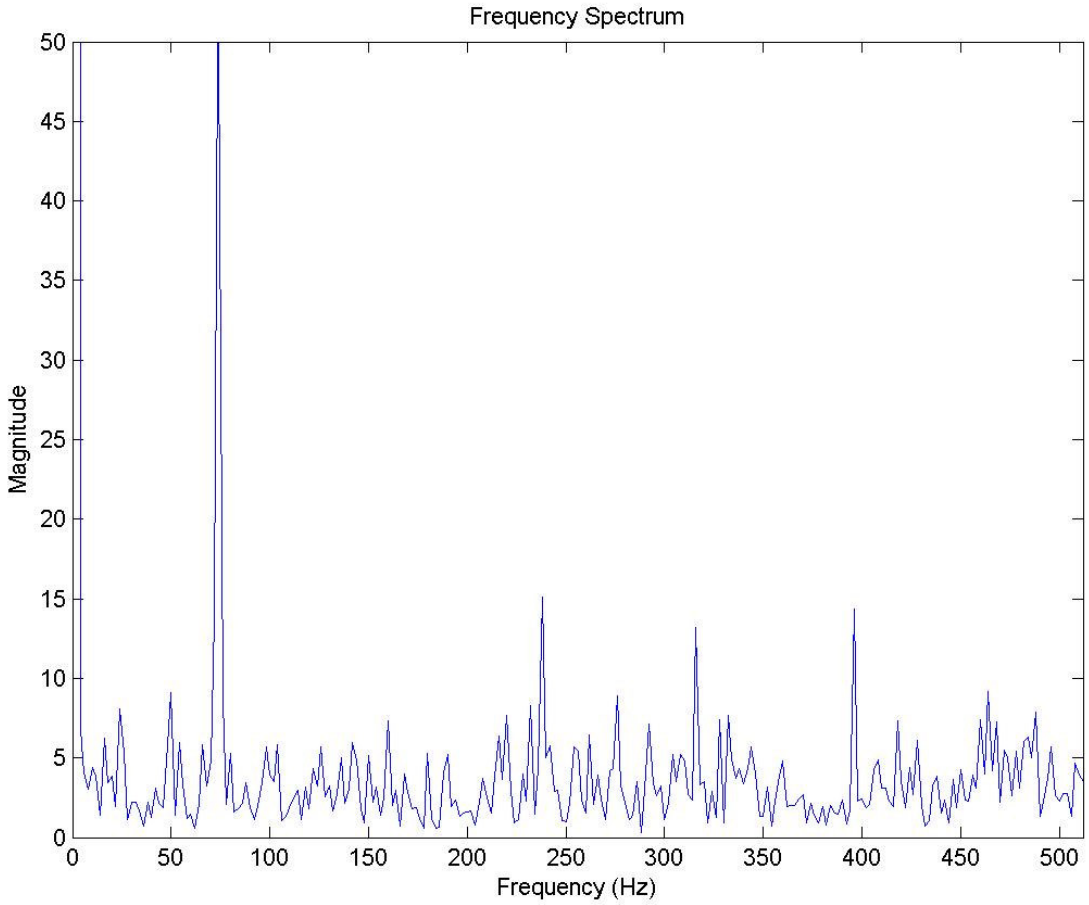

Figure 37: FFT of the Pressure at the Engine Face Plane

When utilizing oscillatory injection, the value of U_{jet} for the calculation of the jet momentum coefficient can be the maximum, root mean square, or mean jet velocity. For this study, the maximum jet velocity was chosen because it allowed for a direct comparison of the flow control authority between steady and unsteady actuation. As discussed earlier, performance limitations of the centrifugal fan cause the mean jet velocity to decrease significantly when pulsing begins. However, the maximum jet velocity during oscillation is identical to the velocity of the steady jet. Therefore, to evaluate the effectiveness of the steady and pulsing actuation modes for a given fan speed (i.e., for a given control input and energy expenditure), the maximum jet velocity is the most practical option for calculating C_{μ}.

A set of experiments were run at a C_{μ} of 0.016 to ascertain the effects of pulsed injection flow control for reduced frequencies of 1.04, 1.39, 1.74, and 2.08. For these tests, only the probe rake was utilized for data acquisition. Figure 38 shows the contours of C_{Ploss} obtained for each of the frequencies, compared to the case of no flow control.

As seen in the contour plots, pulsed blowing at a jet momentum coefficient of 0.016 had little effect on the duct secondary flows. $C_{Ploss,avg}$ only showed improvements of 15.6% with the activation of flow control. Then, for all pulsing frequencies, the value of this parameter remained nearly constant at approximately 43.00. Also, the unsteady actuation induced no reduction in the distortion descriptor. In fact, a slight increase occurred. This poor performance of the pulsing flow control method can be attributed to the decrease in mean jet velocity associated with the fan backpressure limitations

discussed earlier. For future tests, increased jet momentum will be employed, as will higher frequencies.

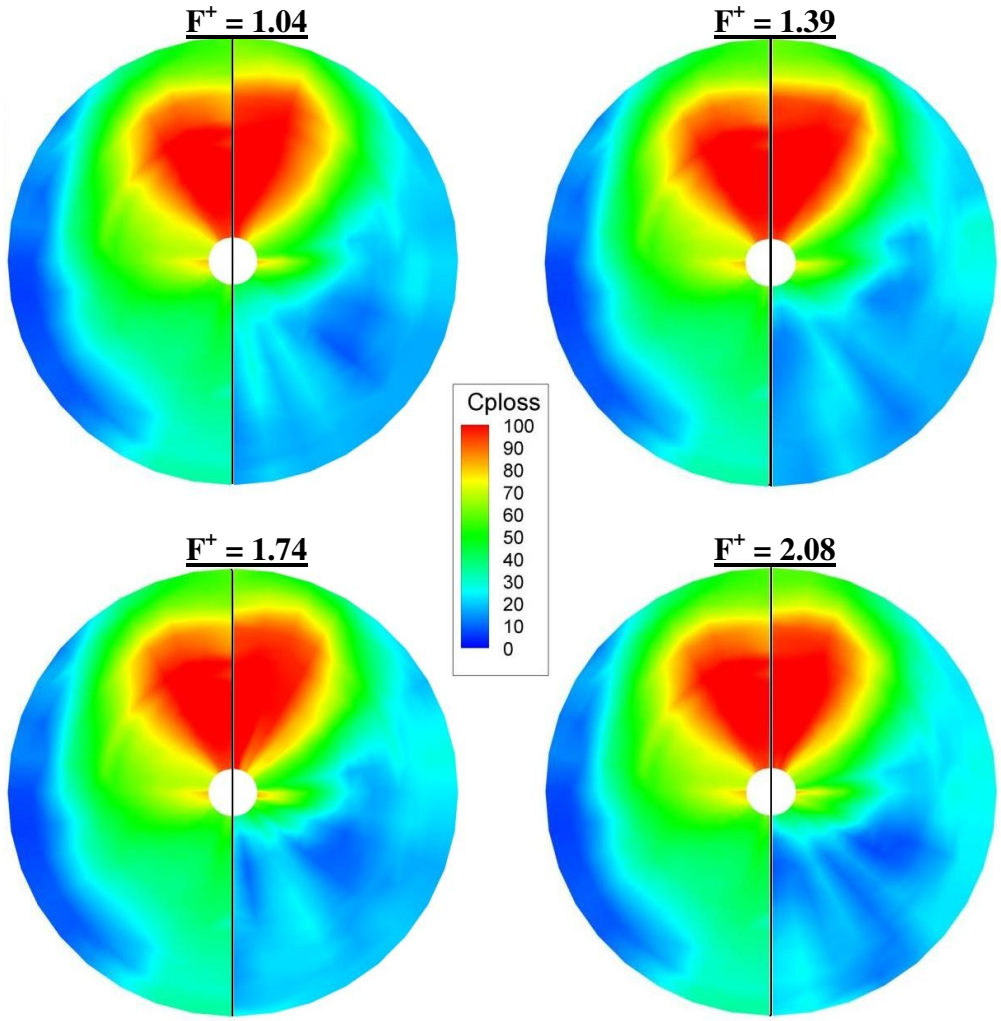

Figure 38: Pressure Loss Coefficient Plots Comparing Various Frequencies of Pulsed Injection (Right Half) to the No Control Case (Left Half)

CONCLUSIONS AND RECOMMENDATIONS

Within this final section, a summary of the results obtained in this document will be presented. Conclusions will be derived from the work, and a set of recommendations for future efforts relating to the research project will be discussed.

Conclusions

A study was performed to gain an understanding of the development and suppression of the secondary flows within a compact, serpentine inlet. Several methods of analysis were employed to characterize the flow mechanics before an investigation was launched to determine the effects of various flow control technologies on the duct performance. The advantages provided by S-shaped inlets include reduced radar cross-section and smaller, lighter, and cheaper air vehicles. The benefits of this study could allow future unmanned aircraft to incorporate this type of jet engine inlet without sacrificing fuel efficiency, engine performance, and longevity.

Experiments run using a baseline duct model revealed the existence of two, large, counter-rotating vortices at the engine face that were produced by the second bend of the inlet. Flow control was instituted at each of the bends of the duct in an attempt to eliminate these vortices. A modular fluidic actuator system was designed to conform to the inlet shape and allow the exploration of three methods of flow control: suction only, suction and steady blowing, and suction and pulsed blowing. Bench top tests showed that, for the slot configuration used in this study, maximum steady jet velocities of just over 40 m/s were possible for sustainable fan speeds. The unsteady injection velocity

distribution demonstrated that the desired sinusoidal variation in velocity was produced by the actuator in pulsing mode.

Control by boundary layer suction delayed separation at each bend and produced improvements in the pressure loss coefficient by 46.8%, 63.4%, and 70.3% for mass flow rates (as a percentage of the core flow rate) of 1.25%, 1.75%, and 2.25%, respectively. However, little change in the size and location of the vortices was observed. Therefore, no substantial decrease in flow distortion was achieved by suction alone. For the case of flow control by suction and steady blowing, a maximum decrease in $C_{Ploss,avg}$ by 37.1% was achieved with a corresponding jet momentum coefficient of 0.024. Also, this control technique changed the position and size of the dominant vortices. As indicated by the reduction in engine face distortion by 41.1%, the flow structures were smaller and closer to the wall with steady suction and injection applied. Finally, when suction and oscillatory injection was utilized, reductions in the pressure loss coefficient of only 16.5% were realized, and the distortion descriptor was actually worsened. The best case of unsteady injection was performed at a reduced frequency of 2.08 and a jet momentum coefficient of 0.016.

In summary, the best performance of the fluidic actuator system in terms of pressure recovery was achieved with just suction at a mass flow percentage of 2.25. When considering both pressure recovery and distortion, suction with steady blowing at a C_{μ} of 0.017 was optimal. However, no level or method of flow control ever produced the required control authority to reduce DC_{60} to the acceptable value of 20% or below. Therefore, further optimization of the flow control actuators will be needed.

Recommendations

Over the course of the research project, several observations were made that could improve the performance of the actuator system. First, the effect of using blowing chamber plates with angled slots needs to be explored. As discussed in the Introduction, it may be necessary to produce a single vortex from the jets to counter the secondary flow formation. Also, a wider spacing of the slots should be investigated. It is possible that the close spacing of the slots utilized in this study caused interference among neighboring jets, thus retarding their vortex development.

A cooling system for the centrifugal fan motors and electronic speed controllers is needed. This apparatus would allow lengthier tests at higher fan speeds. Given the rate of heat build-up observed during testing, directed compressed air should suffice. Additionally, it may be necessary to reevaluate the use of universal joints for linking the rotating slotted shafts. The joints are only rated to 20 Hz, which is much less than the minimum frequency investigated in this survey. In fact, the motors used to drive the shafts can not be operated at less than 30 Hz. To date, no problems have been experienced with the universal joints, but a structural failure during future testing would be a major setback.

Most importantly, it is suggested that an active sensing technique be developed for the application of closed-loop control. The sensing method would have to be noninvasive, and should measure both the jet velocity of the actuators and the state of the flow at the engine face. Recommendations for the measurement devices include hot-film or hot-wire sensors and wall mounted, high frequency pressure sensors.

REFERENCES

[1] Hamstra, J. W., Miller, D. N., Truax, P. P., Anderson, B. A. and Wendt, B. J., "Active Inlet Flow Control Technology Demonstration," ICAS Paper 2000-6.11.2, August 2000.

[2] Anabtawi, A. J., Blackwelder, R. F., Liebeck, R. H. and Lissaman, P. B. S., "Experimental Investigation of Boundary Layer Ingesting Diffusers of a Semi-Circular Cross Section," AIAA Paper 98-0945, January 1998.

[3] MacMartin, D. G., Murray, R. M., Verma. A. and Paduano, J. D., "Active Control of Integrated Inlet / Compressor Systems: Initial Results," FEDSM2001-18275, June 2001.

[4] Anabtawi, A. J., Blackwelder, R. F., Lissaman, P. B. S. and Liebeck, R. H., "An Experimental Study of Vortex Generators in Boundary Layer Ingesting Diffusers with a Centerline Offset," AIAA Paper 99-2110, June 1999.

[5] Reichert, B. A. and Wendt, B. J., "Improving Diffusing S-Duct Performance by Secondary Flow Control," AIAA Paper 94-0365, January 1994.

[6] Vakili, A. D., Wu J. M., Liver, P. and Bhat, M. K., "Experimental Investigation of Secondary Flows in a Diffusing S-Duct," The University of Tennessee Space Institute Technical Report UTSI 86/14, 1984.

[7] Wendt, B. J. and Reichert, B. A., "The Effects of Vortex Ingestion on the Flow in a Diffusing S-Duct," NASA Technical Memorandum 106652, June 1994.

[8] Reichert, B.A. and Wendt, B.J., "An Experimental Investigation of S-Duct Flow Control Using Arrays of Low Profile Vortex Generators," NASA Technical Memorandum 106030, January 1993.

[9] Tindell, R. H., "Highly Compact Inlet Diffuser Technology," *Journal of Propulsion*, Vol. 4, No. 6, pp. 557-563, December 1988.

[10] Kumar, V. and Alvi, F. S., "Use of Supersonic Microjets for Active Separation Control in Diffusers," AIAA Paper 2003-4160, June 2003.

[11] Kumar, V. and Alvi, F. S., "Efficient Control of Separation Using Microjets," AIAA Paper 2005-4879, June 2005.

[12] Anderson, B. H. and Gibb, J., "Study on Vortex Generator Flow Control for the Management of Inlet Distortion," *Journal of Propulsion and Power*, Vol. 9, No. 3, pp. 422-430, June 1993.

[13] Anderson, B. H. and Gibb, J., "Vortex-Generator Installation Studies on Steady-State and Dynamic Distortion," *Journal of Aircraft*, Vol. 35, No. 4, pp. 513-520, August 1998.

[14] Jenkins, L. N., Althoff Gorton, S. and Anders, S. G., "Flow Control Device Evaluation for an Internal Flow with an Adverse Pressure Gradient," AIAA Paper 2002-0266, January 2002.

[15] Harper, D. K., "Boundary Layer Control and Wall-Pressure Fluctuations in a Serpentine Inlet," M.S. Thesis, Mechanical Engineering Department, Virginia Polytechnic Institute and State University, Blacksburg, VA, May 2000.

[16] Bridges, A. and Smith, D. R., "The Influence of Orifice Orientation on the Interaction of a Synthetic Jet with a Turbulent Boundary Layer," AIAA Paper 2001-2774, June 2001.

[17] Collie, W. V., Burgun, R., Heinzen, S. N., Hall Jr., C. E. and Chokani, N., "Advanced Propulsion System Design and Integration for a Turbojet Powered Unmanned Aerial Vehicle," AIAA Paper 2003-0415, January 2003.

[18] Gilarranz, J. L. and Rediniotis, O. K., "Compact, High-Power Synthetic Jet Actuators for Flow Separation Control," AIAA Paper 2001-0737, January 2001.

[19] Gilarranz, J. L., Traub, L. W. and Rediniotis, O. K., "Characterization of a Compact, High-Power Synthetic Jet Actuator for Flow Separation Control," AIAA Paper 2002-0127, January 2002.

[20] Seifert, A. and Pack, L., "Oscillatory Excitation of Unsteady Compressible Flows Over Airfoils at Flight Reynolds Number", AIAA Paper 99-0925, January 1999.

[21] Glezer, A., "Shear Flow Control Using Synthetic Jet Fluidic Actuator Technology," AFOSR Final Technical Report, July 1999.

[22] Amitay, M., Pitt, D., Kibens, V., Parekh, D. and Glezer, A., "Control of Internal Flow Separation Using Synthetic Jet Actuators," AIAA Paper 2000-0903, January 2000.

[23] SAE Committee S-16, Turbine Engine Inlet Flow Distortion, "Aerospace Recommended Practice: Gas Turbine Engine Inlet Flow Distortion Guidelines," ARP 1420, Society of Automotive Engineers, June 1977.

[24] Johansen, E. S., Rediniotis, O. K. and Jones, G., "The Compressible Calibration of Miniature Multi-Hole Probes," *Journal of Fluids Engineering*, Vol. 123, pp. 128-138, March 2001.

[25] Kline, S. J. and McClintock, F. A., "Describing Uncertainties in Single-Sample Experiments," *Mechanical Engineering*, Vol. 75, pp. 3-8, January 1953.

[26] Kerrebrock, J. L., Drela, M., Merchant, A. A. and Schuler, B. J., "A Family of Designs for Aspirated Compressors," ASME 98-GT-196, 1998.

[27] Poisson-Quinton, Ph. and Lepage, L., "Survey of French Research on the Control of Boundary Layer and Circulation," *Boundary Layer and Flow Control*, Vol. 1, Pergamon Press, New York, 1961.

[28] Greenblatt, D. and Wygnanski, I. J., "The Control of Flow Separation by Periodic Excitation," *Progress in Aerospace Sciences*, Vol. 36, pp. 487-545, 2000.

[29] Mittal, R., Kotapati, R. B. and Cattafesta III, L. N., "Numerical Study of Resonant Interactions and Flow Control in a Canonical Separated Flow," AIAA Paper 2005-1261, January 2000.

VITA

Name: Aaron Michael Kirk

Address: H.R. Bright Building, Rm. 701
3141 TAMU
College Station, TX 77843-3141

Education: B.S., Aerospace Engineering, Texas A&M University, 2003
M.S., Aerospace Engineering, Texas A&M University, 2006